Imparting structural robustness of Metal-Organic Cages based on oxo-dimolybdenum clusters

Solène Delaporte[a,b], Isabel Abánades Lázaro[a], Javier López-Cabrelles[a], Eleni C. Mazarakioti[a], Sarah Chebourou[a], Iñigo J. Vitórica-Yrezábal[c], Mónica Giménez-Marqués[a] and Guillermo Mínguez Espallargas*[a]

[a] Instituto de Ciencia Molecular (ICMol), Universitat de València, Catedrático José Beltrán 2, 46980 Paterna, Valencia, Spain
[b] ENS Paris-Saclay, Department de Chimie, 4 Av. des Sciences, 91190 Gif-sur-Yvette, France
[c] School of Chemistry, University of Manchester, Oxford Road, Manchester M13 9PL, United Kingdom

Supporting Information

Table of Contents

S1. Synthesis

All reagents and solvents employed were purchased from Sigma-Aldrich Co and TCI.

Synthesis of MUV-27-py. $Mo_2(OAc)_4$ (40 mg, 0.093 mmol) and BTC (40 mg, 0.19 mmol) were respectively dissolved in 0.8 mL DMF under vigorous stirring at 50 °C. In a 25 mL glass jar, pyridine (2 mL, 24.8 mmol) was mixed with the BTC solution. The mixture turned red upon addition of $Mo_2(OAc)_4$. The jar was heated in an oven at 150 °C for 24 h to give orange crystals mixed with a red gel. The solid was washed with DMF until having a clear solution, and next washed with CH_2Cl_2 (3x2 mL). To ensure a complete solvent exchange, the crystals were immersed in CH_2Cl_2 for 48 h, and then washed with fresh CH_2Cl_2 (3x2 mL) before air drying. Yield: 40 mg (66 %).

Synthesis of MUV-27-py-CH_3. Following the same procedure than **MUV-27-py** synthesis, $Mo_2(OAc)_4$ and BTC were dissolved in 1 mL DMF each and 4-picoline (2 mL, 20.6 mmol, excess) was added to the BTC solution. Orange crystals were obtained after heating 72 h at 120 °C. The same treatment was also applied with DMF and CH_2Cl_2. Yield: 41 mg (63 %).

Synthesis of MUV-27-py-NH_2. $Mo_2(OAc)_4$ (40 mg, 0.093 mmol) and BTC (40 mg, 0.19 mmol) were respectively dissolved in 2 mL DMF under vigorous stirring at 50 °C and next mixed together in a 10 mL glass jar. After heating 18 h at 150 °C in an oven, the dark red solution was mixed with 4-aminopyridine (88 mg, 0.935 mmol) dissolved previously in 1 mL DMF, forming directly a red gel. After heating 4 days at 150 °C in an oven, a mixture of red crystals and red gel was obtained. The solid was washed with DMF until having a clear solution, and next washed with CH_2Cl_2 (3x2 mL). To maximize the solvent exchange, the crystals were immersed in CH_2Cl_2 for 72 h, and then washed with fresh CH_2Cl_2 (3x2 mL) before air drying. Yield: 40 mg (62 %).

Synthesis of MUV-27-bpy-C_2. $Mo_2(OAc)_4$ (80 mg, 0.187 mmol) and BTC (80 mg, 0.38 mmol) were respectively dissolved in 2 mL DMF under vigorous stirring at 50 °C. In a 50 mL glass jar, 1,2-bis(4-pyridyl)ethane (bpy-C_2, 69 mg, 0.37 mmol) was mixed with the BTC solution. The brown solution of $Mo_2(OAc)_4$ was added and the mixture turned directly dark red. Then, the jar was heated in an oven at 80 °C for 72 h to give orange crystals. The solid was washed with DMF until having a clear solution, and next washed with CH_2Cl_2 (3x2 mL). To ensure a complete solvent exchange, the crystals were immersed in CH_2Cl_2 for 72 h, and then washed with fresh CH_2Cl_2 (3x2 mL) before air drying. Yield: 86 mg (66 %).

Synthesis of MUV-27-bpy-C_3. The same procedure than for the synthesis of **MUV-27-bpy-C_2** was followed, using instead 1,3-di(4-pyridyl)propane (bpy-C_3, 148.3 mg, 0.75 mmol). Yield: 65 mg (49 %).

S2. Crystal structures

S2.1. Crystallographic information.

Data collection: X-ray data for compounds **MUV-27-bpy-C_3** and **MUV-27-py** were collected at 150 K on a dual wavelength Rigaku FR-X with Cu-K_α and Mo-K_α radiation equipped with a HypixHE6000 detector and an Oxford Cryosystems nitrogen flow gas system. X-ray data for compounds **MUV-27-py-CH_3**, **MUV-27-bpy-C_2**, **MUV-27-py-NH_2-DMF**, **MUV-27-py-NH_2-DCM** and **MUV-27-py-NH_2-act** were collected at a temperature of 120 K using a Rigaku Supernova with Mo-K_α radiation equipped with a CCD-Eos detector and an Oxford Cryosystems nitrogen flow gas system. Data were collected with CrysAlisPro software.

Crystal structure determinations and refinements. X-ray data were processed and reduced using CrysAlisPro suite of programs. Absorption correction was performed using empirical methods (SCALE3 ABSPACK) based upon symmetry-equivalent reflections combined with measurements at different azimuthal angles. The crystal structures were solved and refined against all F^2 values using the SHELX and Olex2 suite of programmes.[1,2] Despite the highly intense X-ray source, crystals of **MUV-27-py-NH_2-DCM** (1.0 Å), **MUV-27-py-CH_3** (1.0 Å)**, MUV-27-bpy-C_3** (1.17 Å) and **MUV-27-py-NH_2-act** (1.2 Å) present a diffraction limit over 0.83 Å (indicated in parenthesis for each compound).

All atoms in the crystal structures were refined anisotropically except for the hydrogen atoms, solvent molecules and disordered moieties in low-resolution crystals. Hydrogen atoms were placed in the calculated idealized positions for all crystal structures. Disordered DMA^+ cations, solvent molecules and pyridyl ligands in crystal structures were disordered and modelled over two positions. The solvent molecules were constrained to have idealized structure. The atomic displacement parameters (adp) of the ligands have been restrained using similar U_{eq} (SIMU) and rigid bond (RIGU) restraints.

A number of A and B alerts were found, especially for structures **MUV-27-py-NH_2-DCM**, **MUV-27-py-CH_3, MUV-27-bpy-C_3** and **MUV-27-py-NH_2-act** due to the poor resolution obtained and the large disorder found in the crystal structures.

CCDC 2258028-2258034 contain the supplementary crystallographic data for this paper. These data can be obtained free of charge *via* www.ccdc.cam.ac.uk/conts/retrieving.html (or from the Cambridge Crystallographic Data Centre, 12 Union Road, Cambridge CB21EZ, UK; fax: (+44)1223-336-033; or deposit@ccdc.cam.ac.uk).

Table S1. Crystallographic parameters for crystals **MUV-27-py**, **MUV-27-py-CH_3**, **MUV-27-bpy-C_2** and **MUV-27-bpy-C_3**

Identification code	**MUV-27-py**	**MUV27-py-CH_3**	**MUV-27-bpy-C_2**	**MUV-27-bpy-C_3**
Empirical formula	$C_{174}H_{237.05}Mo_{12}N_{34}O_{76}$	$C_{144}H_{164}Mo_{12}N_{20}O_{62}$	$C_{162}H_{189.79}Mo_{12}N_{26}O_{68}$	$C_{170.16}H_{203.26}Mo_{12}N_{14.72}O_{68.72}$
Formula weight	5172.29	4318.22	4740.46	4873.64
Temperature/K	150(1)	120(1)	120(1)	150(1)
Crystal system	triclinic	monoclinic	triclinic	trigonal
Space group	*P*-1	$P2_1/c$	*P*-1	*R*-3
a/Å	19.2467(13)	21.5269(11)	14.5261(7)	39.015(4)
b/Å	19.8669(13)	14.7675(7)	18.4437(10)	39.015(4)
c/Å	19.9079(11)	32.448(2)	20.6426(9)	13.9911(13)
α/°	109.122(5)	90	78.085(4)	90
β/°	104.775(5)	101.313(5)	69.613(4)	90
γ/°	109.834(6)	90	81.101(4)	120
Volume/Å^3	6164.7(7)	10114.8(10)	5051.7(5)	18444(4)
Z	1	2	1	3
ρ_{calc}g/cm^3	1.393	1.418	1.558	1.316
μ/mm^{-1}	0.670	0.794	0.806	5.468
F(000)	2631.0	4336.0	2392.0	7395.0
Crystal size/mm^3	0.05 × 0.02 × 0.02	0.09 × 0.03 × 0.03	0.05 × 0.03 × 0.03	0.61 × 0.02 × 0.02
Radiation	Mo Kα (λ = 0.71073)	Mo Kα (λ = 0.71073)	Mo Kα (λ = 0.71073)	Cu Kα (λ = 1.54184)

2Θ range for data collection/°	3.55 to 50.7	5.608 to 41.63	5.66 to 50.054	4.53 to 82.206
Index ranges	-23 ≤ h ≤ 23, -23 ≤ k ≤ 23, -23 ≤ l ≤ 23	-21 ≤ h ≤ 21, 0 ≤ k ≤ 14, 0 ≤ l ≤ 32	-16 ≤ h ≤ 17, -13 ≤ k ≤ 21, -24 ≤ l ≤ 24	-24 ≤ h ≤ 32, -33 ≤ k ≤ 33, -11 ≤ l ≤ 11
Reflections collected	82214	10579	36477	12642
Independent reflections	22535 [R_{int} = 0.1532, R_{sigma} = 0.1659]	10579 [R_{int} = 0.1500, R_{sigma} = 0.0807]	17806 [R_{int} = 0.0886, R_{sigma} = 0.1917]	2615 [R_{int} = 0.1699, R_{sigma} = 0.1369]
Data/restraints/parameters	22535/63/1150	10579/1706/1217	17806/223/1192	2615/231/278
Goodness-of-fit on F^2	0.970	1.023	0.982	1.035
Final R indexes [I>=2σ (I)]	R_1 = 0.0822 wR_2 = 0.2081	R_1 = 0.1309 wR_2 = 0.3314	R_1 = 0.0735 wR_2 = 0.1306	R_1 = 0.1145 wR_2 = 0.2869
Final R indexes [all data]	R_1 = 0.1858 wR_2 = 0.2613	R_1 = 0.1613 wR_2 = 0.3600	R_1 = 0.1460 wR_2 = 0.1663	R_1 = 0.1744 wR_2 = 0.3268
Largest diff. peak/hole / e Å^{-3}	1.43/–0.88	1.30/–1.18	1.46/–0.90	1.05/–0.46

Table S2. Crystallographic parameters for crystals, **MUV-27-py-NH_2-DMF**, **MUV-27-py-NH_2-DCM** and **MUV-27-py-NH_2-act**

Identification code	**MUV-27-py-NH_2-DMF**	**MUV-27-py-NH_2-DCM**	**MUV-27-py-NH_2-act**
Empirical formula	$C_{143.28}H_{196.96}Mo_{12}N_{35.55}O_{74.36}$	$C_{128.51}H_{154.52}Cl_{13.02}Mo_{12}N_{28}O_{62}$	$C_{133.21}H_{157.62}Mo_{12}N_{32.49}O_{62.98}$
Formula weight	4758.54	4696.27	4372.86
Temperature/K	120(1)	120(1)	120(1)
Crystal system	monoclinic	monoclinic	monoclinic
Space group	$P2_1/n$	$P2_1/n$	$P2_1/n$
a/Å	19.7115(3)	19.3279(4)	19.0877(7)
b/Å	20.0909(2)	19.6862(3)	18.2843(6)
c/Å	27.2180(4)	27.2810(10)	26.7480(7)
α/°	90	90	90
β/°	110.345(2)	109.113(3)	108.715(3)
γ/°	90	90	90
Volume/Å^3	10106.5(3)	9808.0(5)	8841.6(5)
Z	2	2	2
ρ_{calc}g/cm^3	1.564	1.590	1.643
μ/mm^{-1}	0.809	0.998	0.912
F(000)	4809.0	4686.0	4384.0
Crystal size/mm^3	0.06 × 0.04 × 0.02	0.06 × 0.03 × 0.02	0.06 × 0.04 × 0.02
Radiation	Mo Kα (λ = 0.71073)	Mo Kα (λ = 0.71073)	Mo Kα (λ = 0.71073)
2Θ range for data collection/°	5.64 to 50.054	5.594 to 41.632	5.702 to 34.452
Index ranges	-23 ≤ h ≤ 23, -23 ≤ k ≤ 23, -32 ≤ l ≤ 32	-19 ≤ h ≤ 19, -19 ≤ k ≤ 19, -27 ≤ l ≤ 27	-15 ≤ h ≤ 15, -15 ≤ k ≤ 15, -22 ≤ l ≤ 22
Reflections collected	167847	190947	102160
Independent reflections	17832 [R_{int} = 0.1207, R_{sigma} = 0.0766]	10244 [R_{int} = 0.1428, R_{sigma} = 0.0586]	5318 [R_{int} = 0.1320, R_{sigma} = 0.0487]
Data/restraints/parameters	17832/651/1158	10244/734/1109	5318/306/658
Goodness-of-fit on F^2	1.039	1.062	1.047
Final R indexes [I>=2σ (I)]	R_1 = 0.0664 wR_2 = 0.1711	R_1 = 0.0871 wR_2 = 0.2255	R_1 = 0.0810 wR_2 = 0.2114
Final R indexes [all data]	R_1 = 0.1134 wR_2 = 0.2050	R_1 = 0.1231 wR_2 = 0.2524	R_1 = 0.1136 wR_2 = 0.2415
Largest diff. peak/hole / e Å^{-3}	1.44/–0.71	1.41/–0.97	0.81/–0.51

S2.2 General features

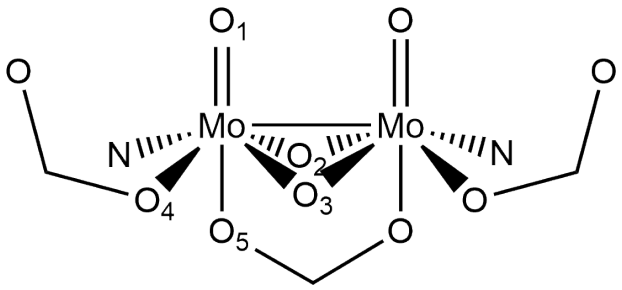

Figure S1. SBU of **MUV-27**.

Table S3. Selection of distance ranges (in Å) in the different members of the **MUV-27** family

MUV-27	py	py-CH_3	py-NH_2	bpy-C_2	bpy-C_3
Mo–Mo	2.547-2.555	2.550-2.558	2.545-2.557	2.549-2.553	2.553
Mo–O(1)	1.679-1.690	1.629-1.732	1.676-1.694	1.691-1.705	1.701-1.744
Mo–O(2)	1.932-1.940	1.940-1.965	1.929-1.950	1.931-1.942	1.857-1.882
Mo–O(3)	1.922-1.928	1.935-1.997	1.929-1.946	1.921-1.946	1.875-1.898
Mo–O(4)	2.071-2.098	2.061-2.112	2.069-2.111	2.077-2.095	2.001-2.042
Mo–O(5)	2.252-2.277	2.248-2.308	2.243-2.296	2.253-2.296	2.242-2.273
Mo–N	2.234-2.250	2.213-2.241	2.184-2.219	2.222-2.245	2.228-2.237

S2.3 Crystal structure of MUV-27-py

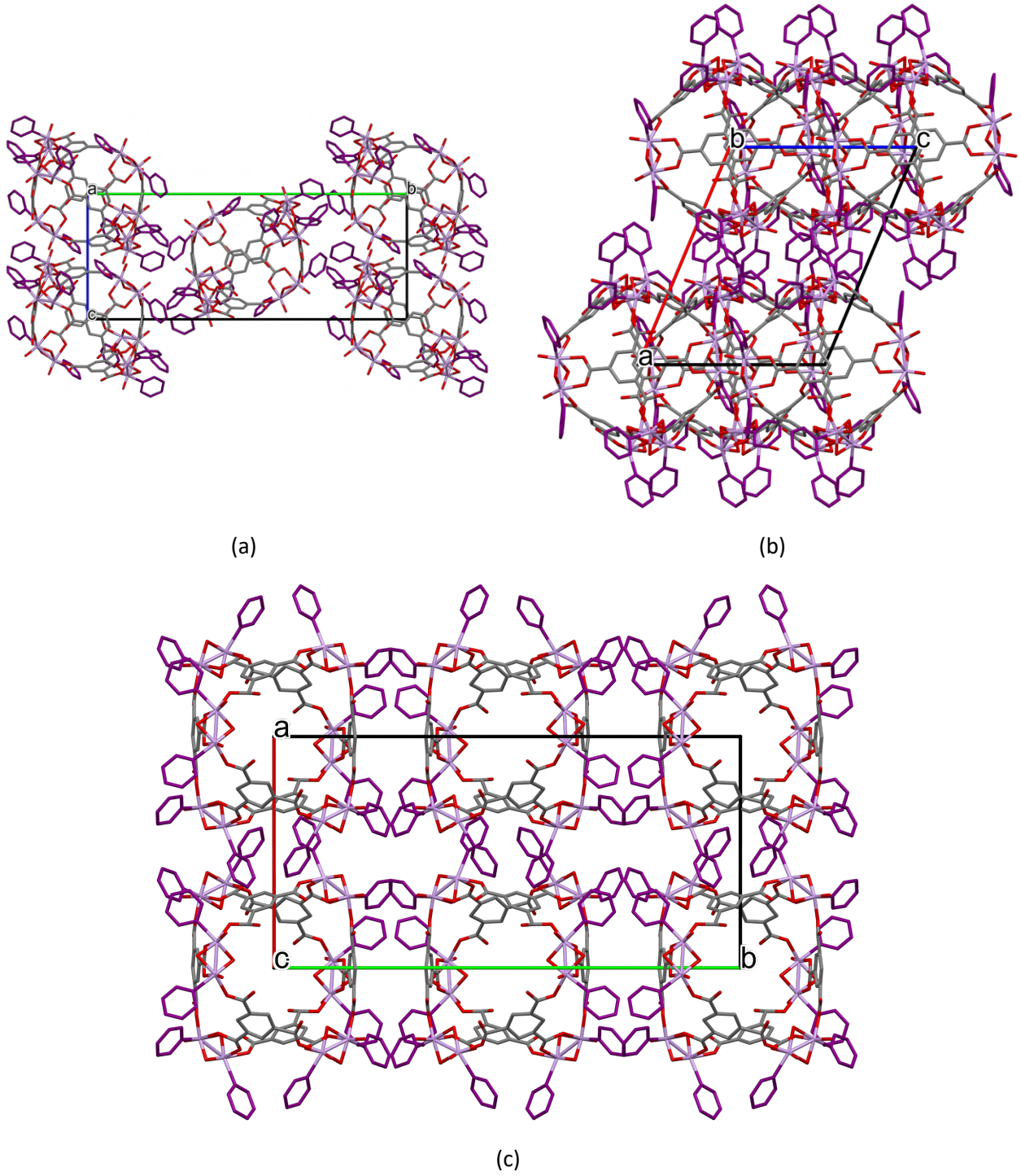

Figure S2. Crystal-packing of **MUV-27-py** viewed along view along the *a*-axis (a), the *b*-axis (b) and the *c*-axis (c). Mo = pink, O = red, C = grey. The capping ligand (pyridine) is shown in purple. Hydrogen atoms and solvent molecules have been omitted for clarity.

S2.4 Crystal structure of MUV-27-py-CH_3

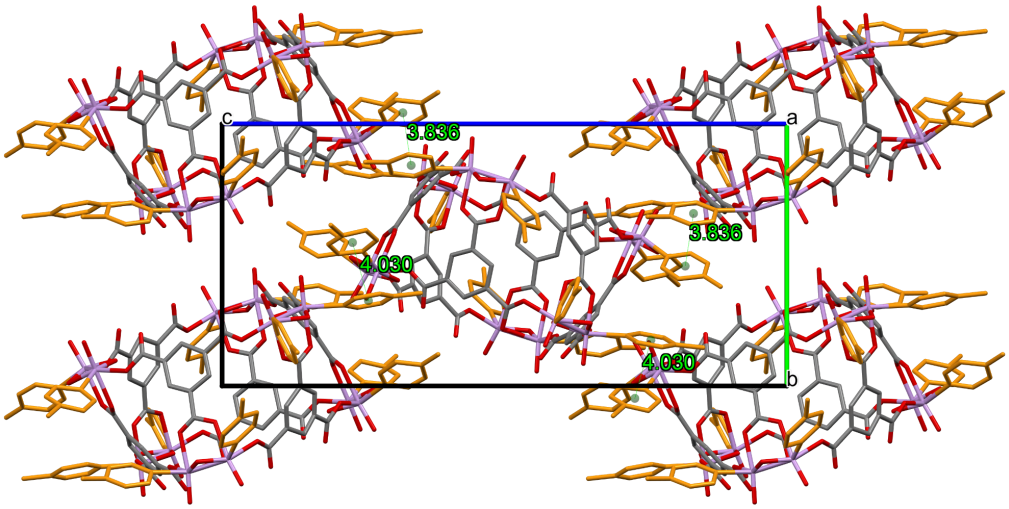

(a)

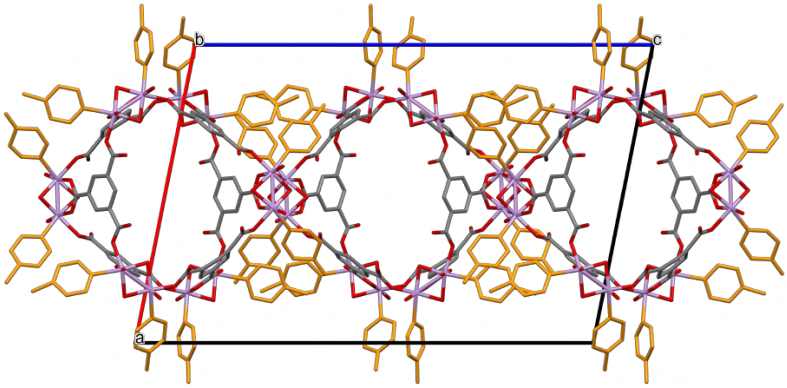

(b)

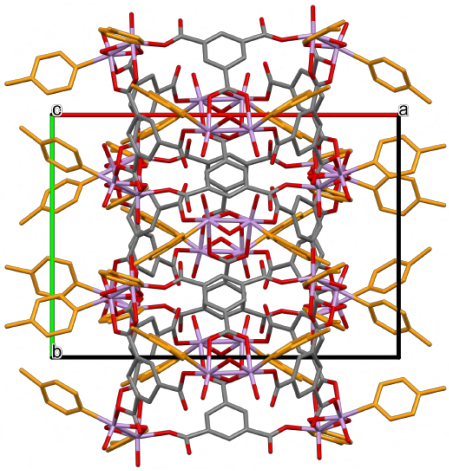

(c)

Figure S3. Crystal-packing of **MUV-27-py-CH_3** viewed along view along the *a*-axis (a), the *b*-axis (b) and the *c*-axis (c). Mo = pink, O = red, C = grey. The capping ligand (4-methylpyridine) is shown in orange. Hydrogen atoms and solvent molecules have been omitted for clarity.

S2.5 Crystal structure of MUV-27-py-C_2

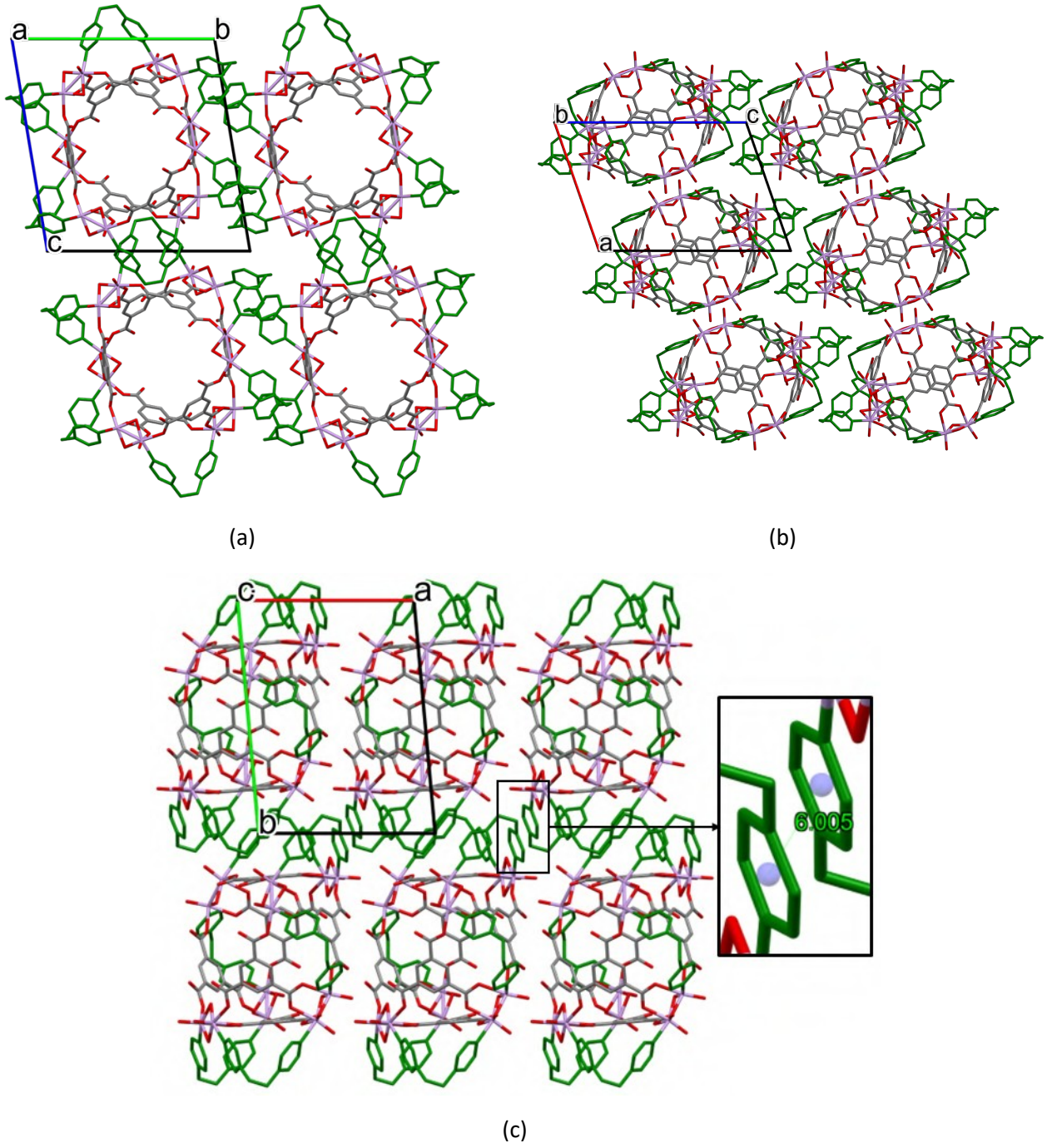

Figure S4. Crystal-packing of **MUV-27-bpy-C_2** viewed along view along the *a*-axis (a), the *b*-axis (b) and the *c*-axis (c). Mo = pink, O = red, C = grey. The capping ligand (ethane-4,4'-bipyridine) is shown in green. Hydrogen atoms and solvent molecules have been omitted for clarity.

S2.6 Crystal structure of MUV-27-py-C_3

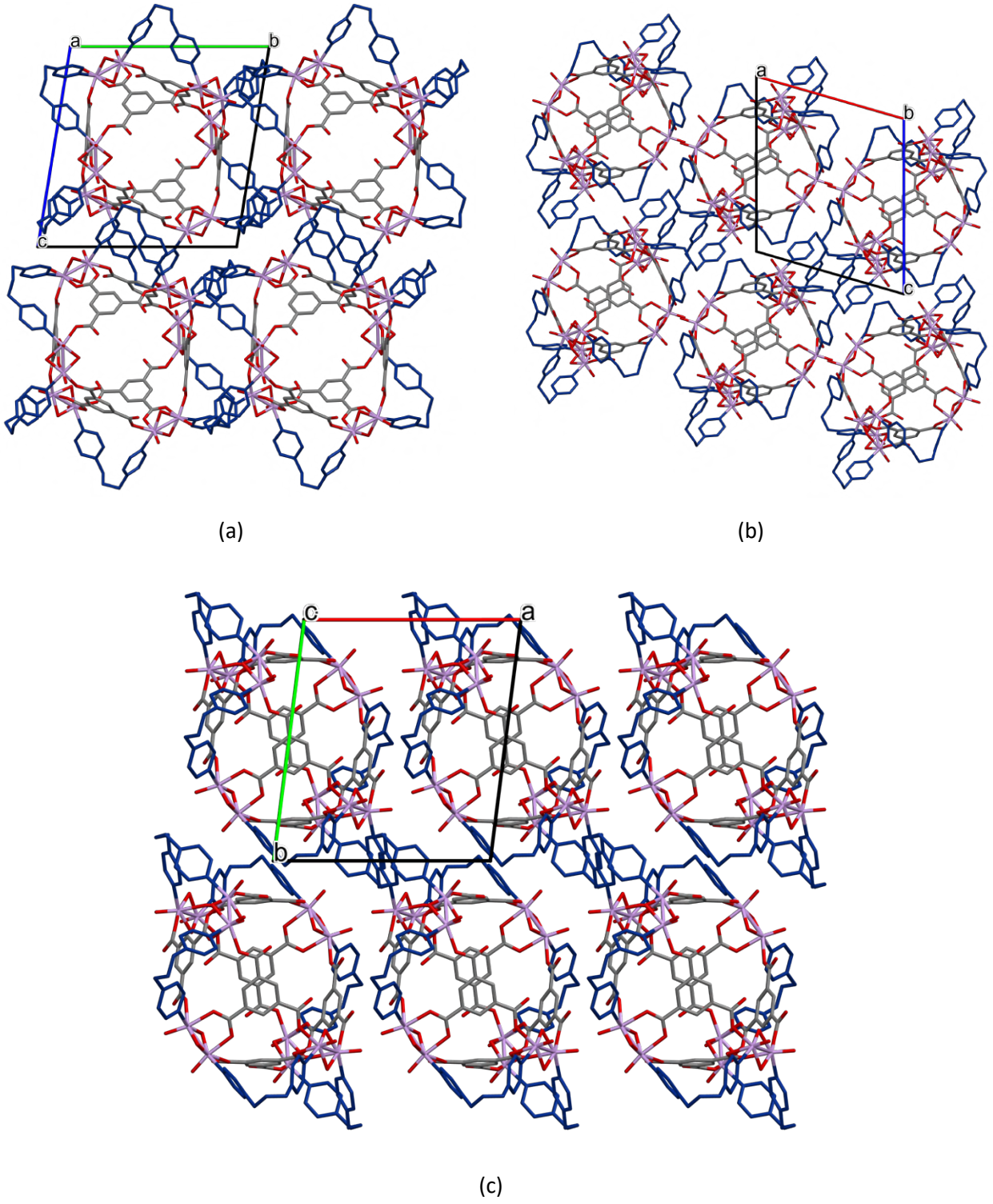

(a) (b)

(c)

Figure S5. Crystal-packing of **MUV-27-bpy-C_3** viewed along view along the *a*-axis (a), the *b*-axis (b) and the *c*-axis (c). Mo = pink, O = red, C = grey. The capping ligand (propane-4,4'-bipyridine) is shown in dark blue. Hydrogen atoms and solvent molecules have been omitted for clarity.

S2.7 Crystal structure of MUV-27-py-NH_2

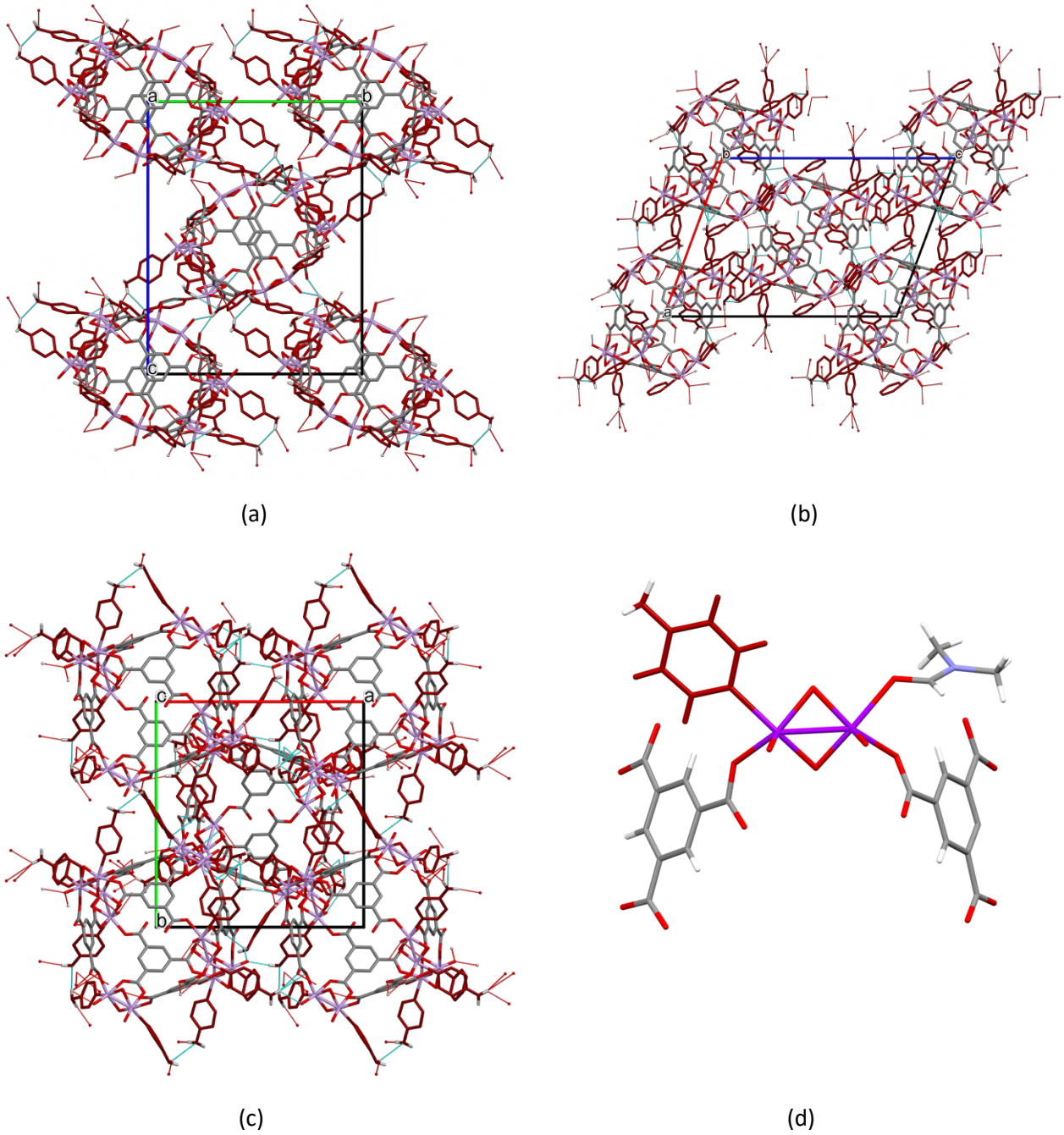

Figure S6. Crystal-packing of **MUV-27-py-NH_2** viewed along view along the *a*-axis (a), the *b*-axis (b) and the *c*-axis (c). (d) Coordination of DMF molecule to one Mo-atom in one of the 6 Mo_2O_4 units. H-bonds are shown as red dotted lines. Mo = pink, O = red, C = grey. The capping ligand (4-aminopyridine) is shown in dark red. Hydrogen atoms and solvent molecules have been omitted for clarity except those of the NH_2 groups.

SXRD measurements have been conducted on **MUV-27-py-NH$_2$** crystals to investigate the crystallographic changes upon activation. Measurements showed that the space group remains $P2_1/n$ after solvent exchange (DCM), and activation (act.). The evolution of the unit cell parameters are depicted in Table S5, and the changes observed in distances within the cage and the crystal packing in Table S6. The corresponding distances reported in Table S6 are illustrated on Figure S7. Overall, a decrease of the unit cell parameters occurred, and the cages centroid get closer together upon activation, but no degradation of the MOCs was observed.

Table S5. Unit cell parameters of **MUV-27-py-NH$_2$**.

	DMF	CH_2Cl_2	act.
a (Å)	19.7115(3)	19.3279(4)	19.0877(7)
b (Å)	20.0909(2)	19.6862(3)	18.2843(6)
c (Å)	27.2180(4)	27.2810(10)	26.7480(7)
α (°)	90	90	90
β (°)	110.345(2)	109.113(3)	108.715(3)
γ (°)	90	90	90

Table S6. Parameters extracted from SXRD of **MUV-27-py-NH$_2$**.

Distances (Å)	**DMF**	**DCM**	**Act.**
Mo–Mo	2.5479-2.5579	2.5483-2.5509	2.5301-2.5569
Cavity diameter (D_c)	10.2770-11.1899	10.3019-10.9454	9.8913-11.0639
Adjacent Mo_2 metallic clusters (A_{Mo})	12.130-12.455	12.184-12.450	12.117-12.619
Opposite Mo_2 metallic clusters (O_{Mo})	15.397-15.899	15.404-15.813	15.045-15.893
cage1 - cage2	21.828	21.510	20.867
cage1 - cage3	17.028	17.030	16.480

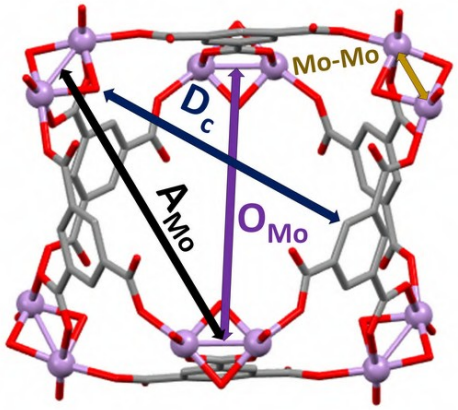

(a)

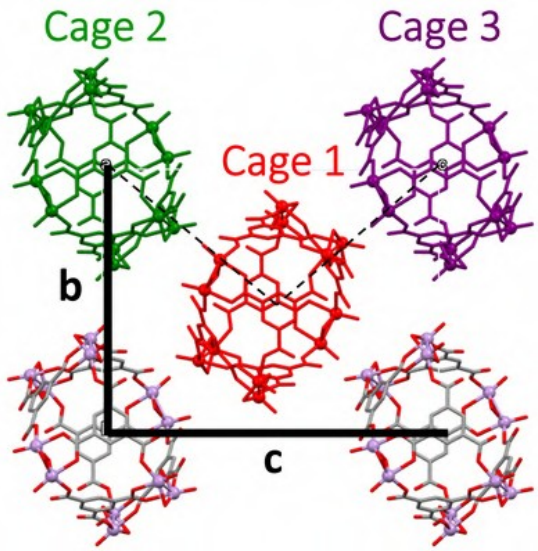

(b)

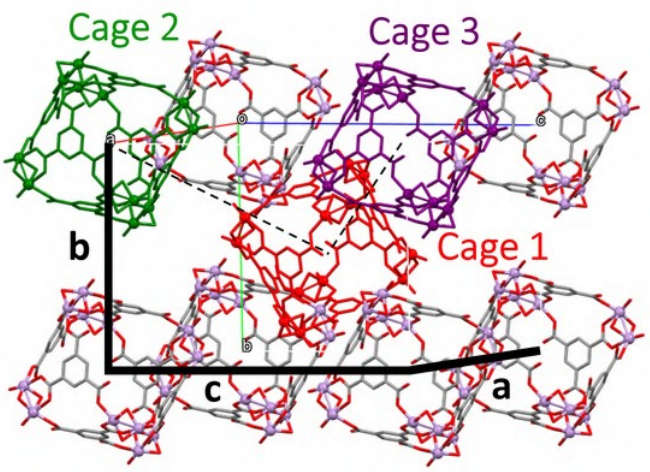

(c)

Figure S7. Illustration of the distances extracted from SXRD of **MUV-27-py-NH_2**.

S3 Powder X-ray diffraction

All materials were characterized by X-ray powder diffraction. The samples were lightly ground in an agate mortar and pestle and used to fill 0.5 mm borosilicate capillaries that were mounted and aligned on an Empyrean PANalytical powder diffractometer, using Cu K_α radiation (λ = 1.54056 Å). Repeated measurements were collected at room temperature in the range 2θ = 3–20 ° and merged into a single diffractogram. Each material was washed with DMF and dried under vacuum prior to the XRPD measurement. It can be seen that upon drying the MOCs a change in the crystal structure occurs except in the case of **MUV-27-py-NH_2**.

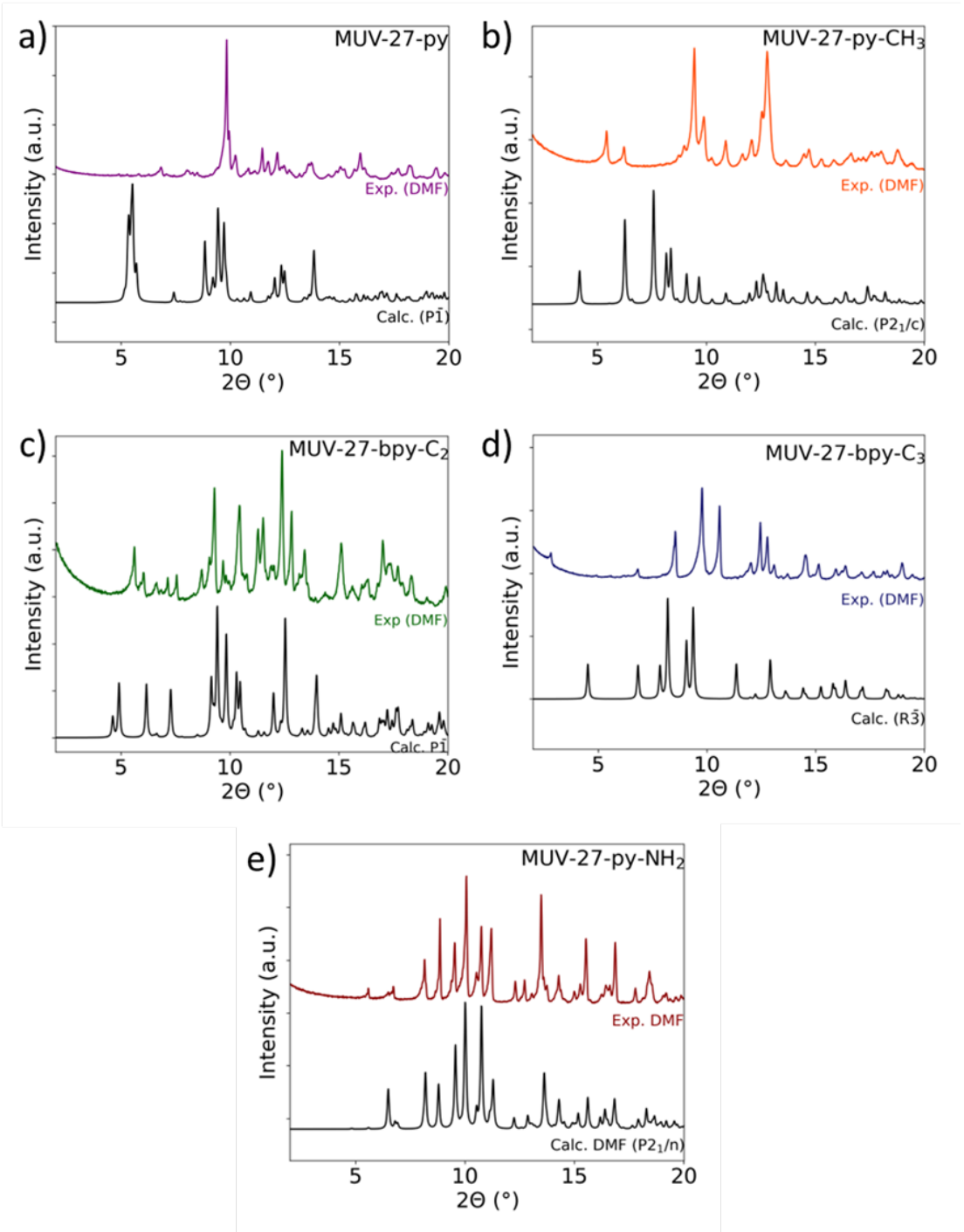

Figure S8. PXRD of as-synthesized **MUV-27**.

S4 Optical images

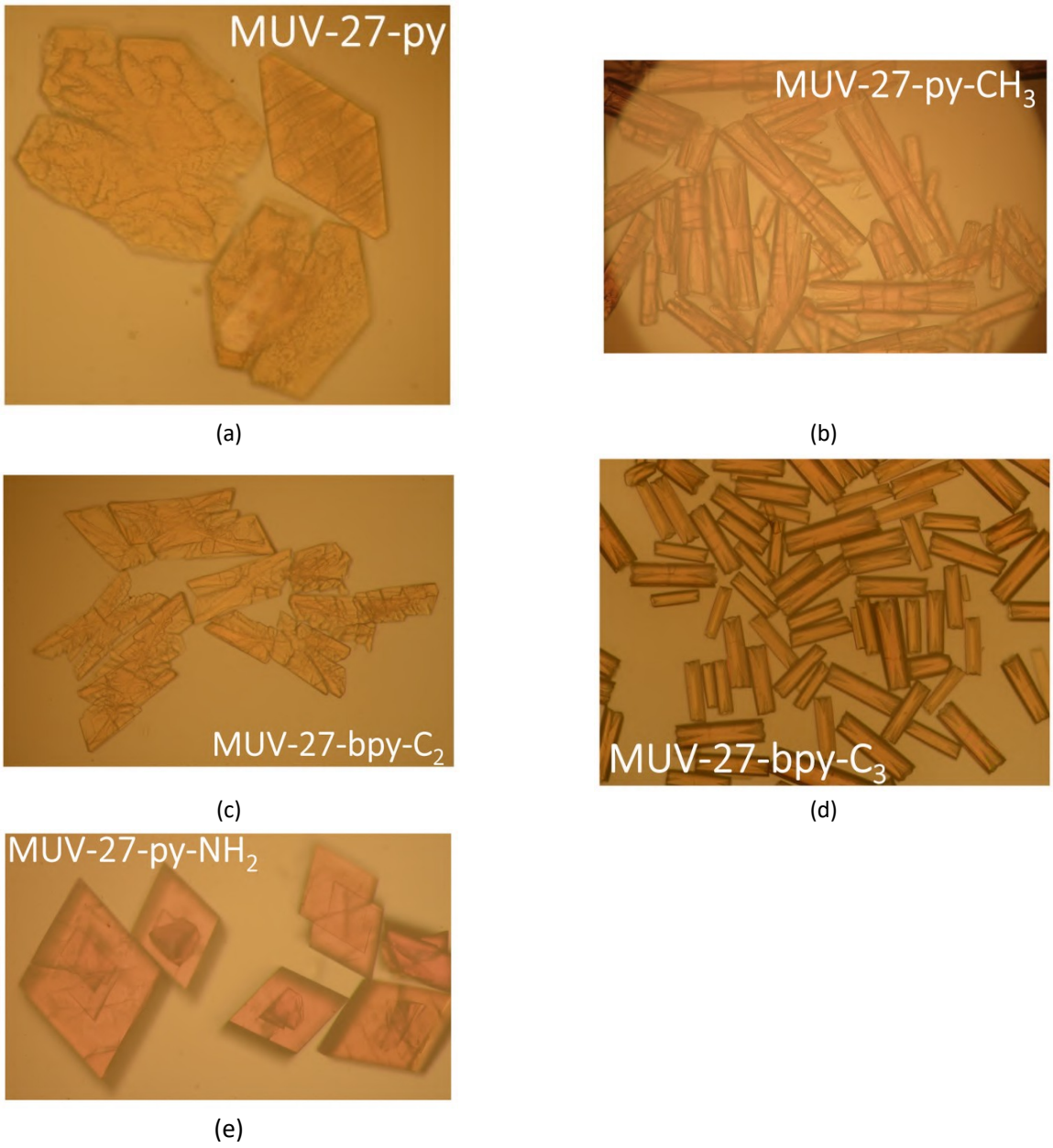

Figure S9. Optical images of different crystals of **MUV-27** in DMF: a) **MUV-27-py**; b) **MUV-27-py-CH$_3$**; c) **MUV-27-bpy-C$_2$**; d) **MUV-27-bpy-C$_3$**; e) **MUV-27-py-NH$_2$**.

S5 Infrared spectroscopy

Fourier Transform Infrared Spectroscopy of solids was collected using a Shimadzu Fourier Transform Infrared Spectrometer, FTIR-8400S, fitted with a Diamond ATR unit. Infra-red (IR) spectra of the starting reactants and all **MUV-27** washed with DMF and dried under vacuum overnight are presented on Figures S10 –S12.

As illustrated on Figure S12, the aliphatic ν (C–H) bands around 3050 cm^{-1} are observed for all **MUV-27** MOCs. The presence of DMA^+ is deduced from the weak signal at *ca*. 2790 cm^{-1}associated with the $\nu(NH^+)$ stretching vibration. Concerning **MUV-27-py-NH_2**, two additional distinctive bands at 3334 and 3207 cm^{-1} are attributed to the -NH_2 stretching modes of the 4-aminopyridine ligands.[3]

The 1900–300 cm^{-1} region provides more information about the coordinated ligands and remaining solvent. First, the strong band around 1640 cm^{-1} attested the presence of DMF within the materials, corresponding to the ν(C=O) stretching frequency. Secondly, for the BTC linker mainly $\nu COO^-,as$ and $\nu COO^-,s$ (as = asymmetric and s = symmetric) stretching modes of the carboxylate groups can be predicted. In our case, the BTC ligands present two different coordination modes to the Mo: syn,syn and monodentate, with $\Delta\nu_{syn,syn} \approx 198$ cm^{-1} and $\Delta\nu_{mono} > 198$ cm^{-1} ($\Delta\nu = 198$ cm^{-1} for the sodium salt Na_3BTC).[4] Thus, the strong bands in the range of 1628-1610 cm^{-1} have been attributed to $\nu COO^-,as$. Then, the two bands at 1430-1415 cm^{-1} and 1340-1329 cm^{-1} are ascribed to $\nu COO^-,s$. All BTC stretching frequencies and corresponding $\Delta\nu$ are reported in Table S2.

Finally, the bands in the 1300-300 cm^{-1} fingerprint region can be attributed to pyridine and BTC stretching and bending modes. Two intense bands present in all the materials around 900 cm^{-1} are ascribed to the vibrational stretching modes ν(Mo=O)[5] whereas the Mo-O-Mo stretching modes appear around 702 cm^{-1}.

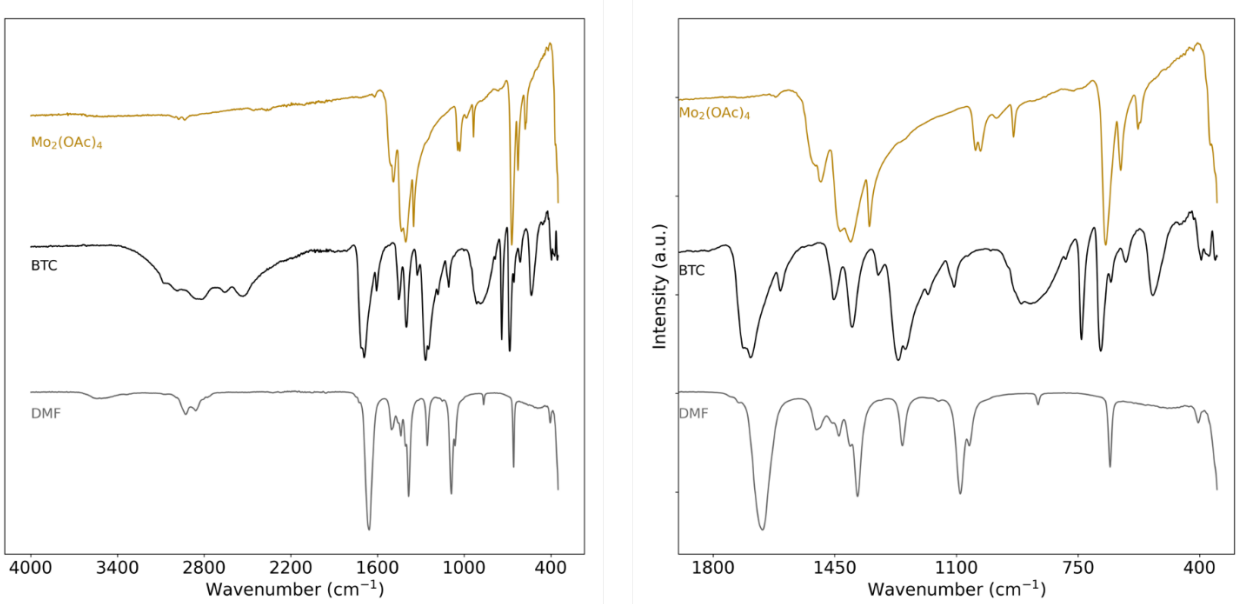

Figure S10. IR of the ligands used in **MUV-27** syntheses.

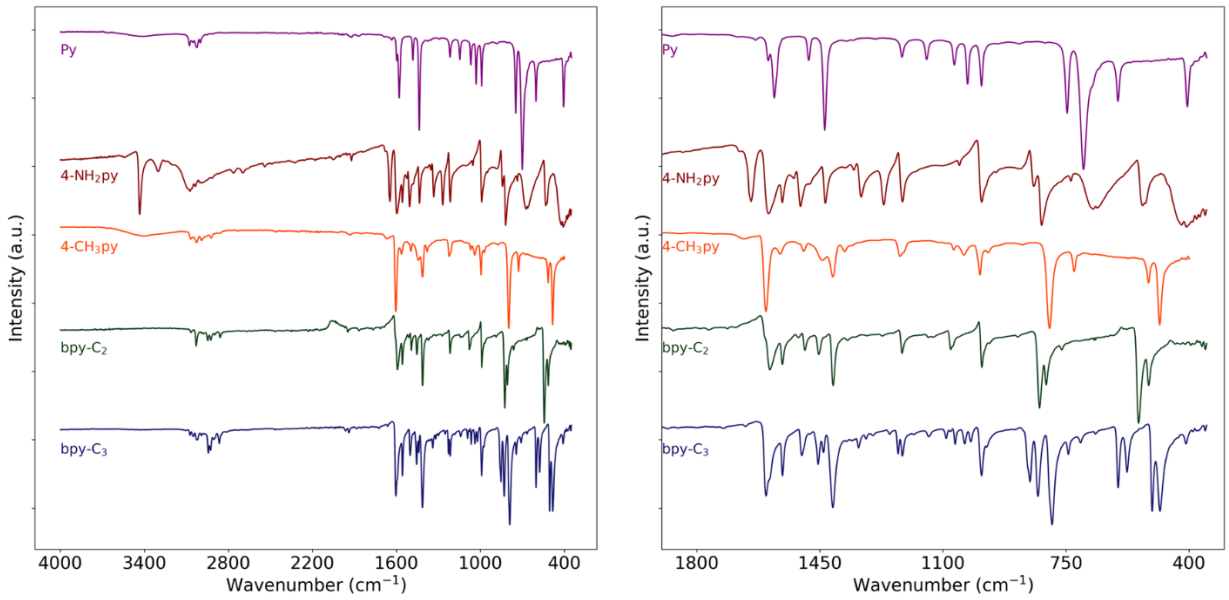

Figure S11. IR of the reactants used in **MUV-27** syntheses.

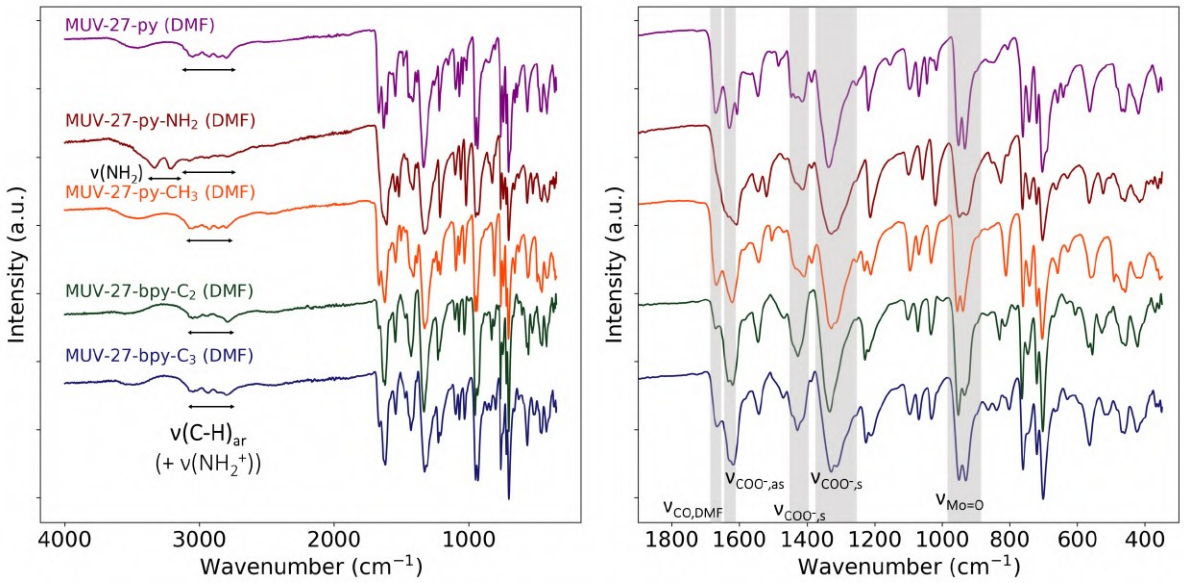

Figure S12. IR of **MUV-27 (DMF)**.

Table S7. νCOO^- (cm^{-1}) in **MUV-27** with BTC coordination modes.

	syn,syn mode			monodentate mode	
MUV-27	νCOO_{a-s}	νCOO_{s-}	$\Delta\nu$	νCOO_{s-}	$\Delta\nu$
Py	1627	1418	209	1330	297
py-CH_3	1623	1429	194	1341	282
py-NH_2	1635	1419	216	1329	306
bpy-C_2	1621	1428	193	1339	282
bpy-C_3	1615	1427	188	1335	282

S6 Nuclear Magnetic Resonance

Nuclear Magnetic Resonance (NMR) spectra were recorded on a Bruker AVIII 300 MHz spectrometer and referenced to residual solvent peaks (DMSO-d_6 2.5 ppm).

^{1}H NMR of **MUV-27** MOCs have been conducted after digestion of the materials, by adding 5 drops of D_2SO_4 in 0.5 mL of DMSO-d_6. It allowed us to probe the chemical purity and composition of the samples with the ligands ratio, solvents and impurity traces.

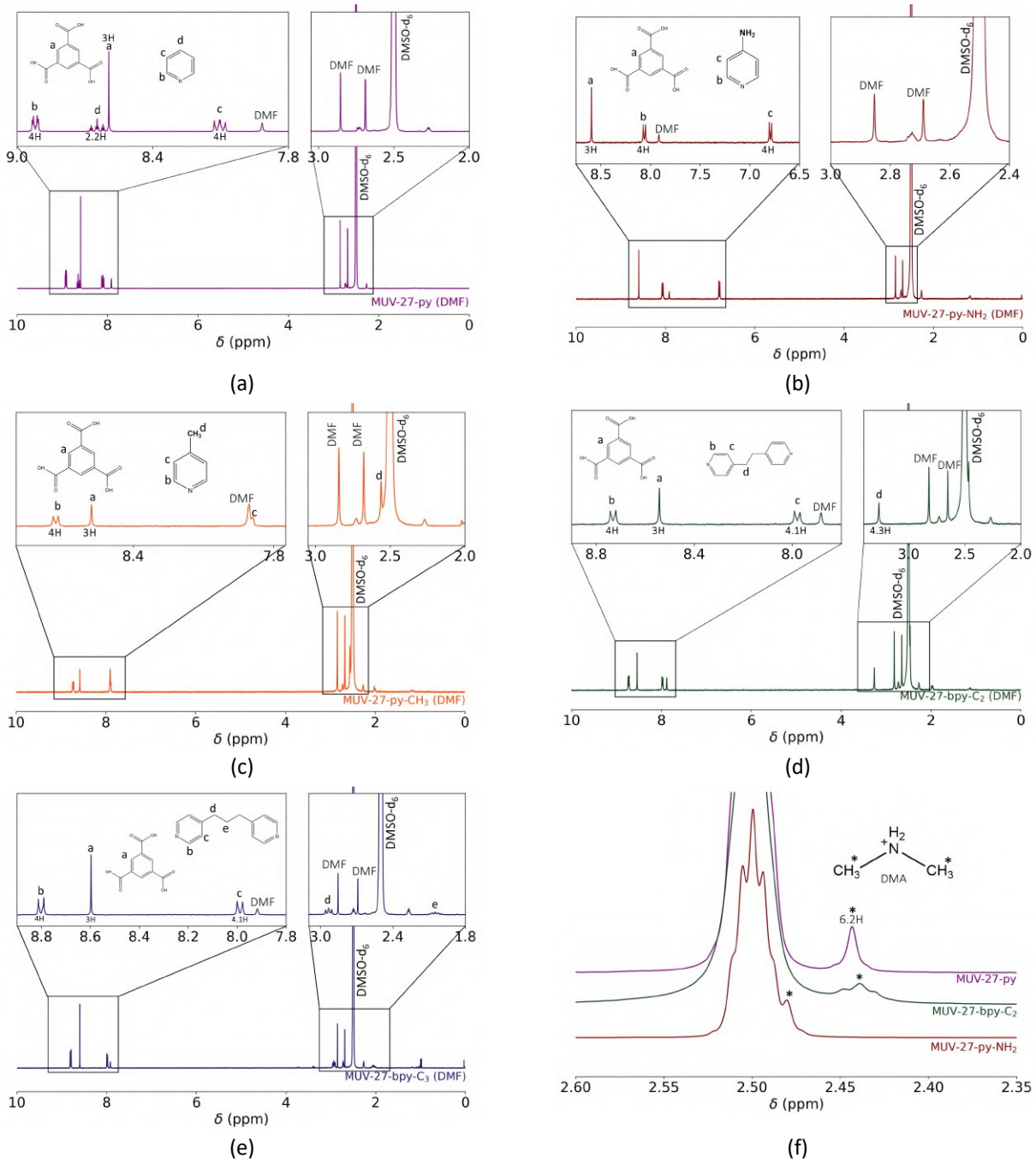

Figure S13. ^{1}H NMR spectra (DMSO-d_6 and D_2SO_4, 300 MHz) of: a) **MUV-27-py**; b) **MUV-27-py-NH$_2$**; c) **MUV-27-py-CH$_3$**; d) **MUV-27-bpy-C$_2$**; e) **MUV-27-bpy-C$_3$**; f) detailed region of the NMR spectra of **MUV-27-py**, **MUV-27-bpy-C$_2$** and **MUV-27-py-NH$_2$**, where the signals corresponding to DMA^+ cations can be observed.

The ligands ratios were measured to confirm the composition of the MOCs. We expected either a py-X/BTC ratio of 2, or a bpy-C_x/BTC ratio of 1, based on the SXRD structures. The integrations were normalized to the BTC singlet peak (3H), giving then integrations of the terminal ligands' protons in agreement with the expected ratio.

The SXRD structures of **MUV-27** MOCs also indicated the presence of DMA^+ cations in the cavity. According to a previous study, the ^1H NMR signal of the DMA^+ methyl groups should appear around 2.4 ppm in acidified DMSO-d_6.[6] However, in most of the recorded NMR, no signals were observed as it was probably hidden in the DMSO peak at 2.5 ppm. Nevertheless, it was possible to distinguish a signal in some spectra, probably because of variable shift, depending on the quantity of acid added. As shown on Figure S13f, this signal could be detected for **MUV-27-py**, **MUV-27-py-NH_2** and **MUV-27-bpy-C_2**, but the integration was not possible for the last two, due to the proximity of the solvent peak. The singlet at 2.44 ppm in the **MUV-27-py** spectrum was far enough to be integrated, indicating the presence of one DMA^+ molecule per BTC, i.e. 6 DMA^+ cations per cage.

S7 Thermogravimetric Analysis

Thermogravimetric Analysis (TGA) was carried out on as-synthetized materials with a Mettler Toledo TGA/SDTA 851 apparatus between 25 and 700 °C under ambient conditions (10 °C min^{-1} scan rate and an airflow of 9 $mL \cdot min^{-1}$). The mass decrease around 150 °C for can be attributed to the removing of DMF. All MOCs show an appreciable thermal stability with a degradation start around 160°C.

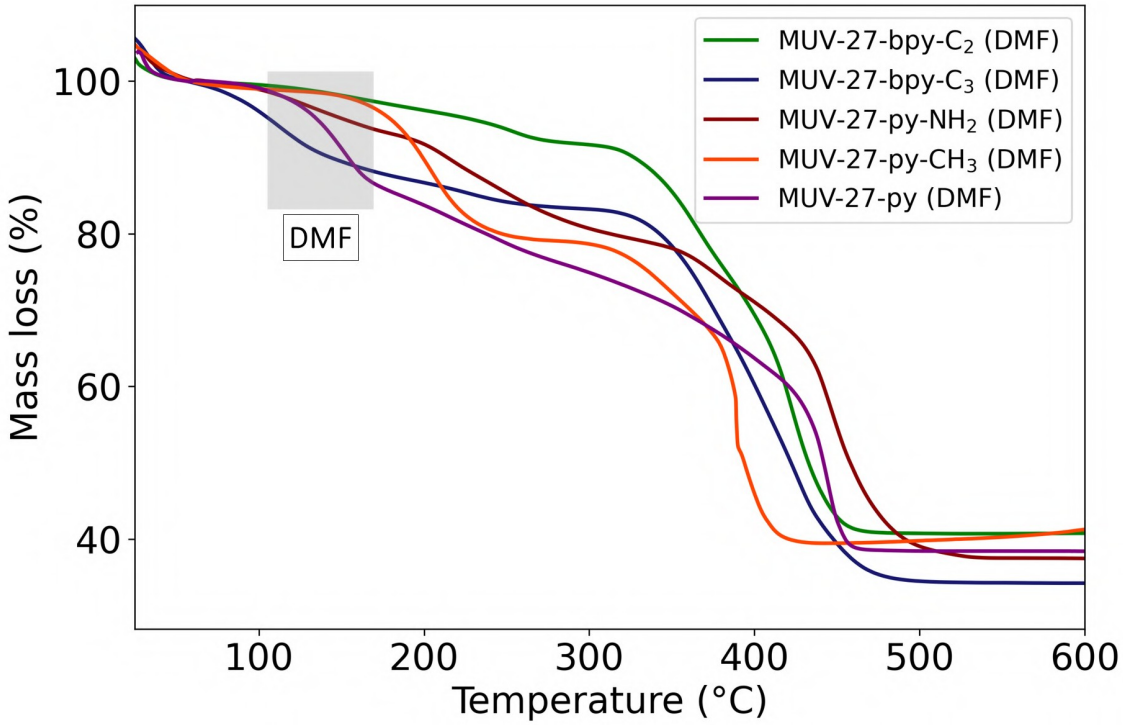

Figure S14. TGA of MUV-27 (DMF).

S8 UV-visible spectroscopy

UV-visible spectroscopy of the materials in solution was collected using a UV-Vis-NIR spectrophotometer (V-670 Jacso). Solution samples were prepared by dissolving the solid in DMSO upon stirring (0.1 mM), measurements were conducted on freshly prepared solutions.

The optical properties of the cages in solution have also been investigated. In this purpose, we performed UV-visible spectroscopy measurements on orange solutions of **MUV-27-py, -py-CH$_3$** and **-bpy-C$_3$**, in 0.1 mM DMSO. The measurements are displayed on Figure S15 with those of $Mo_2(OAc)_4$ and BTC as comparison (0.6 mM). An intense absorption band is observed at 323 nm (**MUV-27-bpy-C$_3$**), and 315 nm (**MUV-27-py** and **MUV-27-py-CH$_3$**), that can be ascribed to charge transfer. A less intense band is also present at 480 nm.

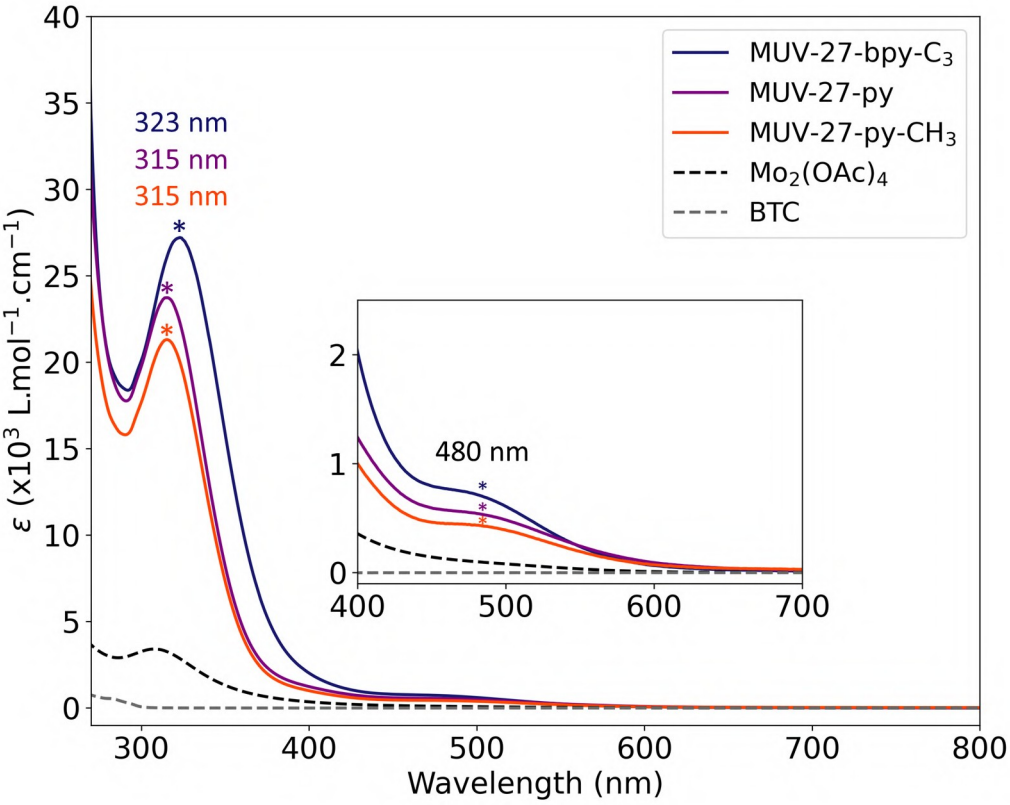

Figure S15. UV-Vis of **MUV-27-py**, **MUV-27-py-CH$_3$** and **MUV-27-bpy-C$_3$** in 0.1 mM DMSO, $Mo_2(OAc)_4$ and BTC in 0.6 mM DMSO.

S9 Chemical and thermal stability

S9.1 Structural changes

The crystallinity of the MOCs has been examined after solvent exchange. Experimental PXRD patterns of solvated and activated materials, with calculated patterns, are depicted on Figure S16

While **MUV-27-py** and **MUV-27-bpy-C$_3$** retained their initial crystallinity upon solvent exchange, **MUV-27-py-CH$_3$**, **MUV-27-py-NH$_2$** and **MUV-27-bpy-C$_2$** PXRD patterns exhibited some changes.

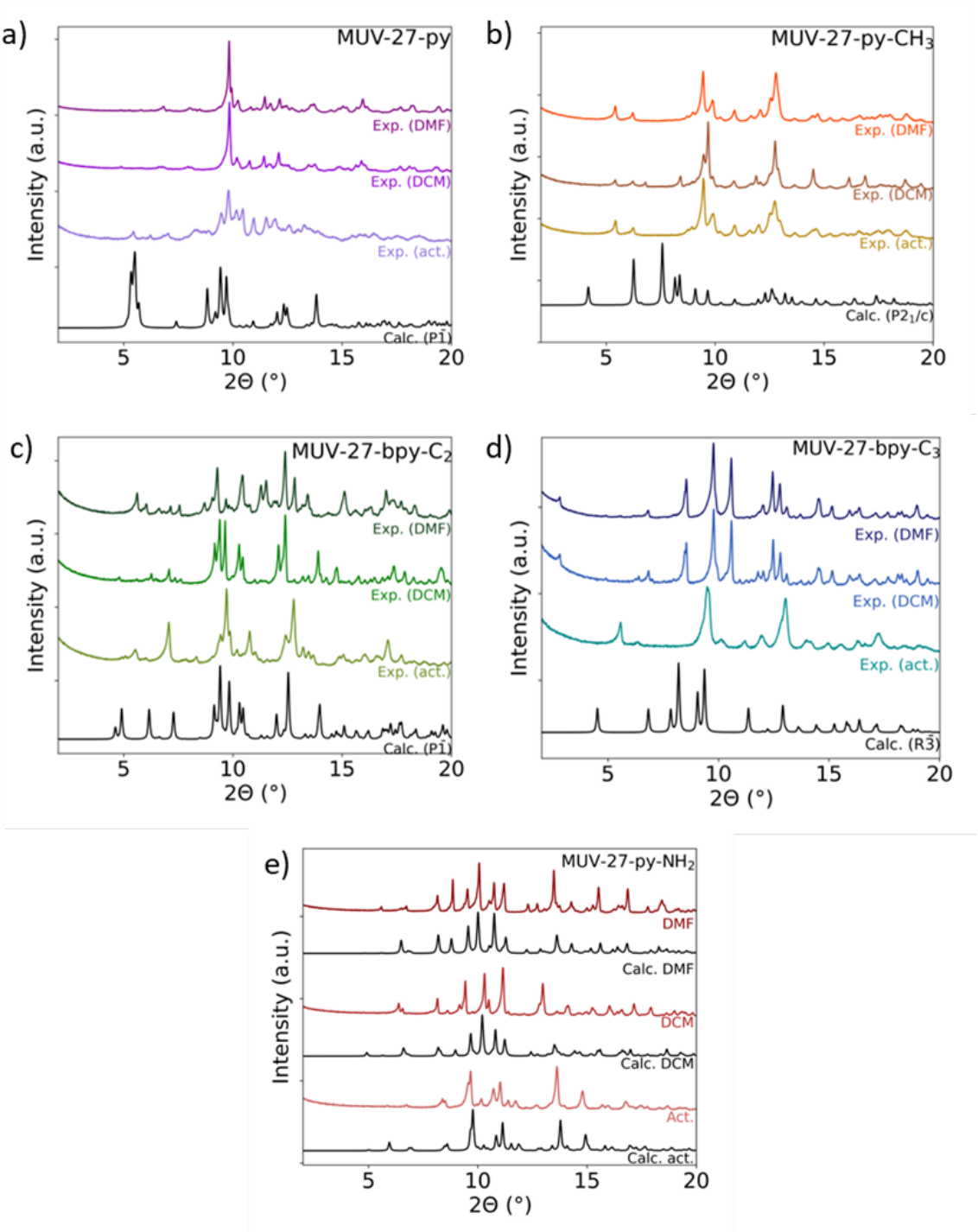

Figure S16. PXRD of all **MUV-27** either washed with DMF, DCM or activated.

S9.2 FT-IR spectroscopy

FT-IR spectra of **MUV-27 (DMF)** and **MUV-27 (act.)** are depicted on Figure S17. First, we can notice the disappearance of the DMF strong band around 1640 cm^{-1}, which confirms their well- activation. However, the solvent exchange was more difficult to monitor for **MUV-27-py-NH$_2$** due the presence of a coordinated DMF molecule that is not exchanged. We can also point out that no modification appeared on the IR spectra before and after activation, indicating the absence of chemical alteration upon activation.

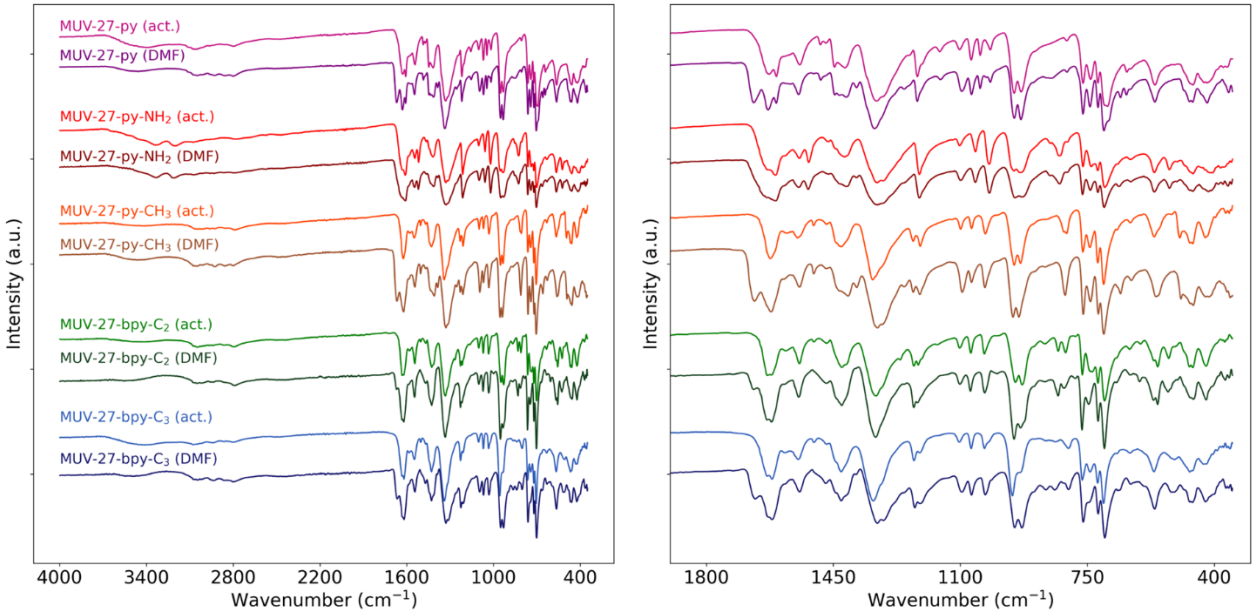

Figure S17. IR of **MUV-27 (act.)** and (DMF).

S9.3 Acid-digested ^{1}H-NMR of activated samples

The activation of **MUV-27** was also followed with acid-digested ^{1}H NMR (Figures S18 to S22). The complete activation was confirmed with the absence of signals corresponding to DMF (ca. 7.9 ppm), and DCM (ca. 5.7 ppm) for the activated **MUV-27**, except **MUV-27-py-NH$_2$**, in which 1 DMF molecule per cage remains present. This is in agreement with other data, as one DMF is coordinated to a metal centre.

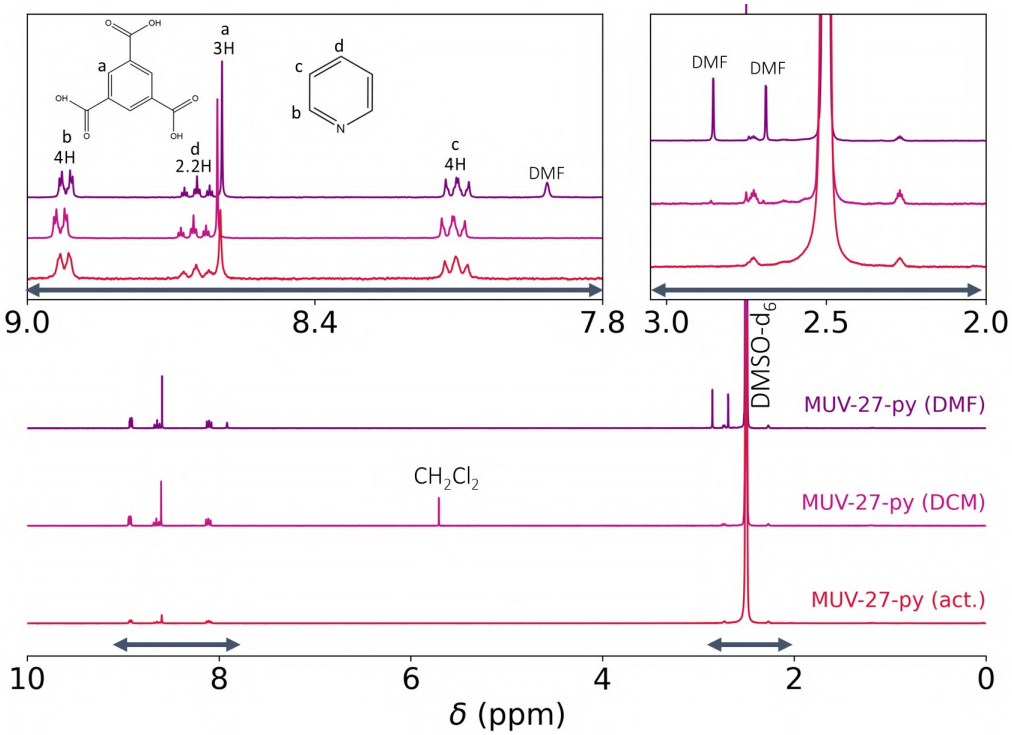

Figure S18. ^{1}H NMR spectra of **MUV-27-py** (DMSO-d_6 and D_2SO_4, 300 MHz)

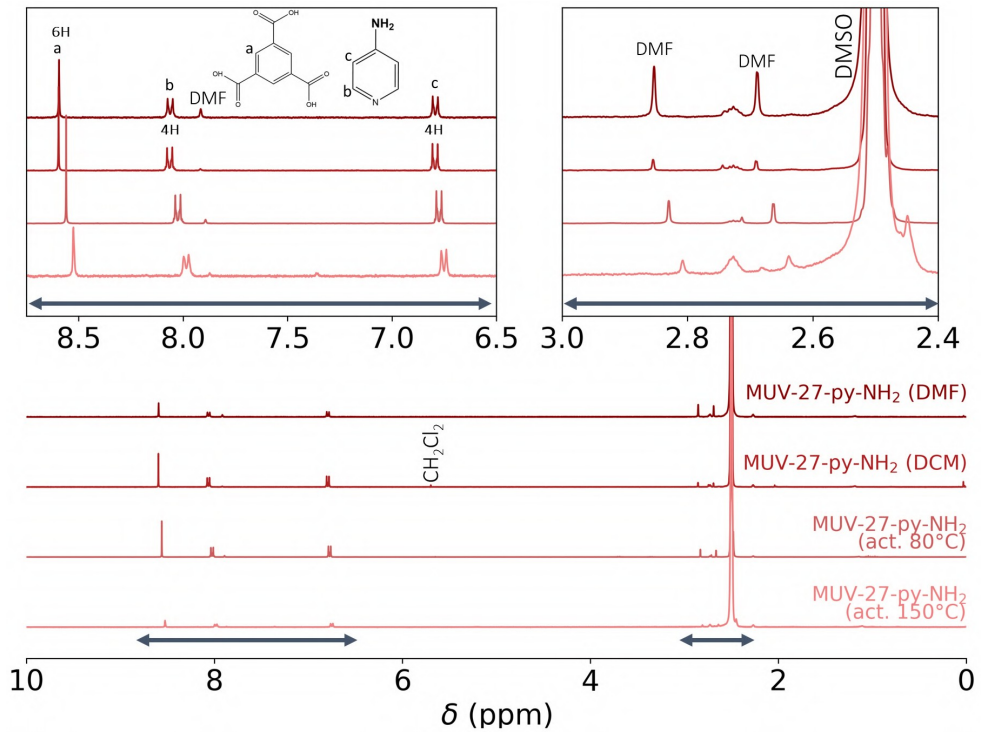

Figure S19. ^{1}H NMR spectra of **MUV-27-py-NH$_2$** (DMSO-d_6 and D_2SO_4, 300 MHz)

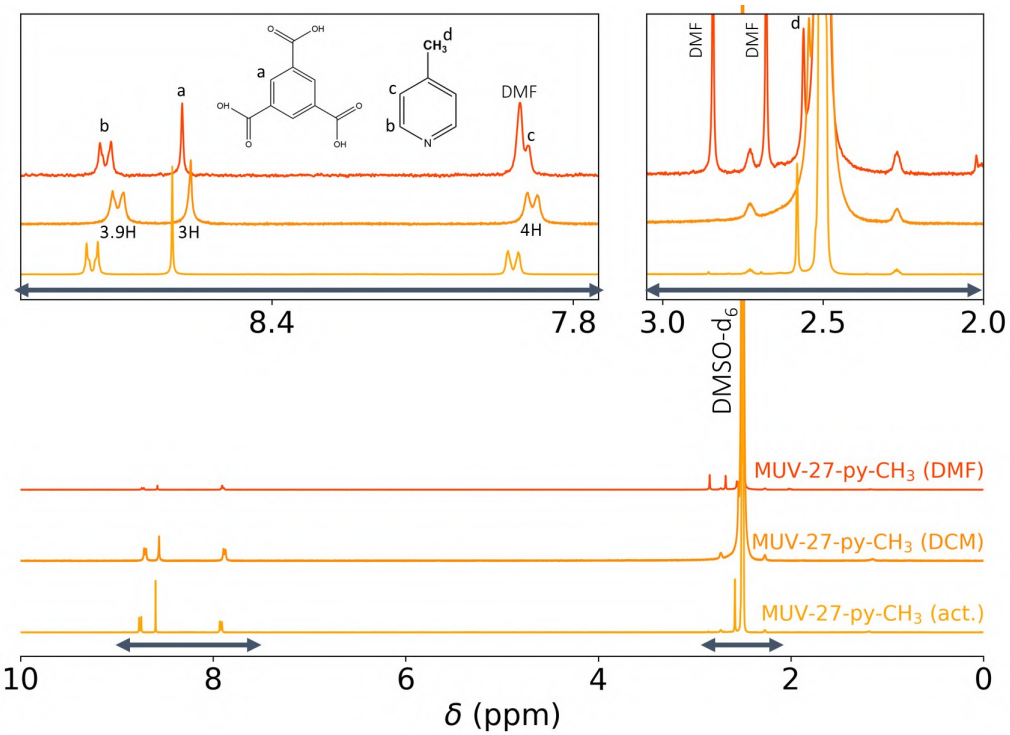

Figure S20. ^{1}H NMR spectra of **MUV-27-bpy-CH$_3$** (DMSO-d$_6$ and D_2SO_4, 300 MHz)

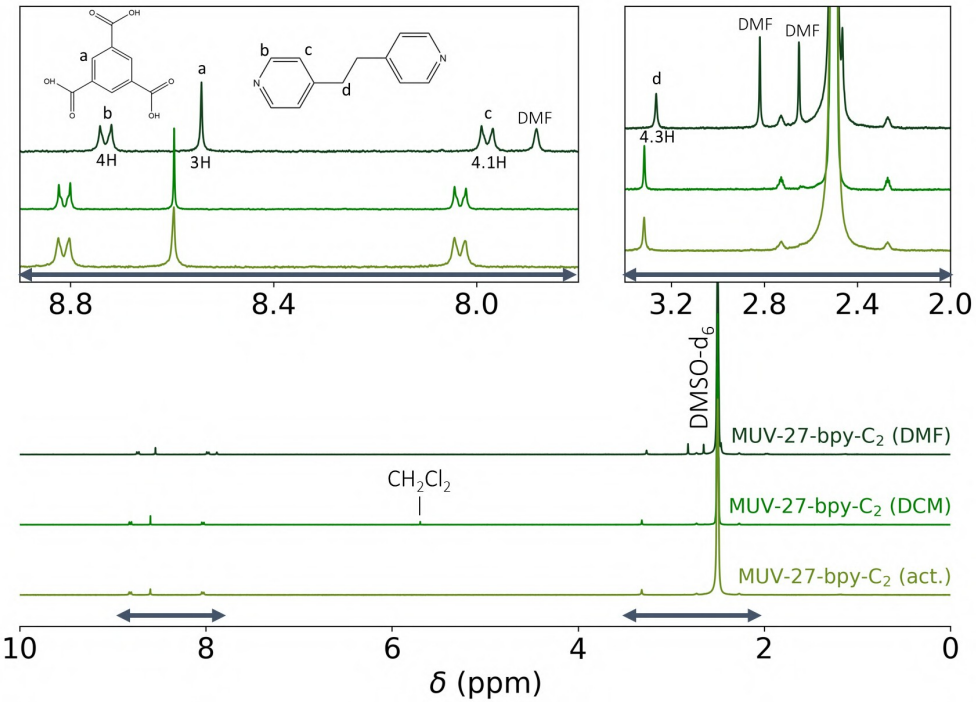

Figure S21. ^{1}H NMR spectra of **MUV-27-bpy-C$_2$** (DMSO-d$_6$ and D_2SO_4, 300 MHz)

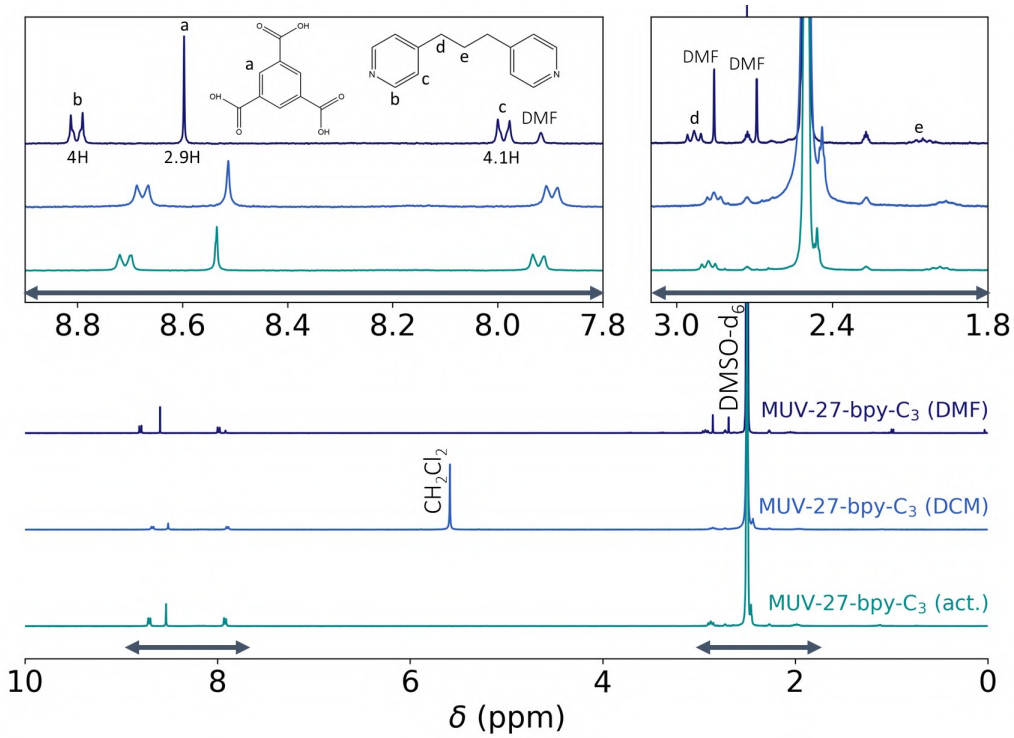

Figure S22. ^{1}H NMR spectra of **MUV-27-bpy-C$_3$** (DMSO-d$_6$ and D_2SO_4, 300 MHz)

S9.4 ^{1}H-NMR of cages in solution

The solubility of **MUV-27** has been investigated in diverse organic solvents (DMSO, CH_3CN, H_2O), being only soluble in DMSO. However, we noticed a poor stability in time of **MUV-27** in DMSO, with the solution turning blue after a few days. The ^{1}H NMR of **MUV-27** in DMSO-d$_6$are illustrated in Figures S23 to S26, with those of free H_3BTC and terminal ligands as comparison.

It can be observed the presence of signals corresponding to free py-X or bpy-C$_x$, that are highlighted in grey in Figures S23 to S26, revealing a partial decoordination of the pyridine ligands. However, additional signals are also present for **MUV-27- bpy-C$_2$** and **MUV-27-bpy-C$_3$** (Figures S25 and S26), that can be attributed to the bipyridine coordinated to the molybdenum centres.

The formation of the cage is also confirmed by the signal of the BTC ligand: the free ligand gives rise to a singlet at 8.6 ppm, but the cages present a triplet (integrated to 1 H) and a doublet (integrated to 2 H) coupled together (J ≈ 1.7 Hz), which is in agreement with the BTC coordinated to Mo atoms within **MUV-27**, with two chemically equivalent protons and another inequivalent.

A broad peak is also observed around 2 ppm, which can be ascribed to DMA^+ cations.

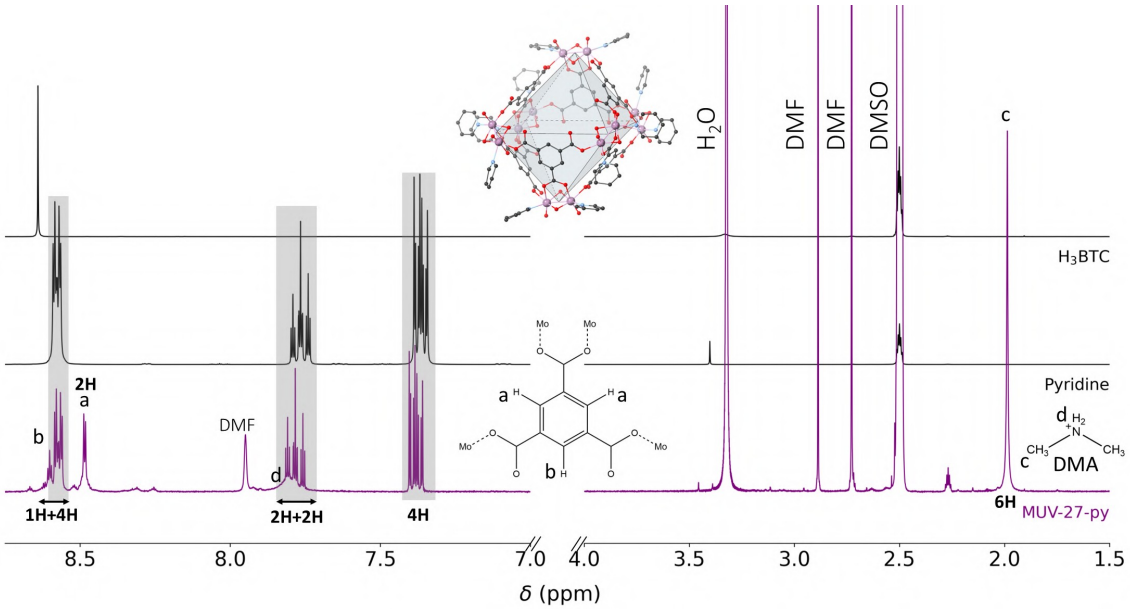

Figure S23. ^{1}H NMR of **MUV-27-py** (DMSO-d_6, 300 MHz).

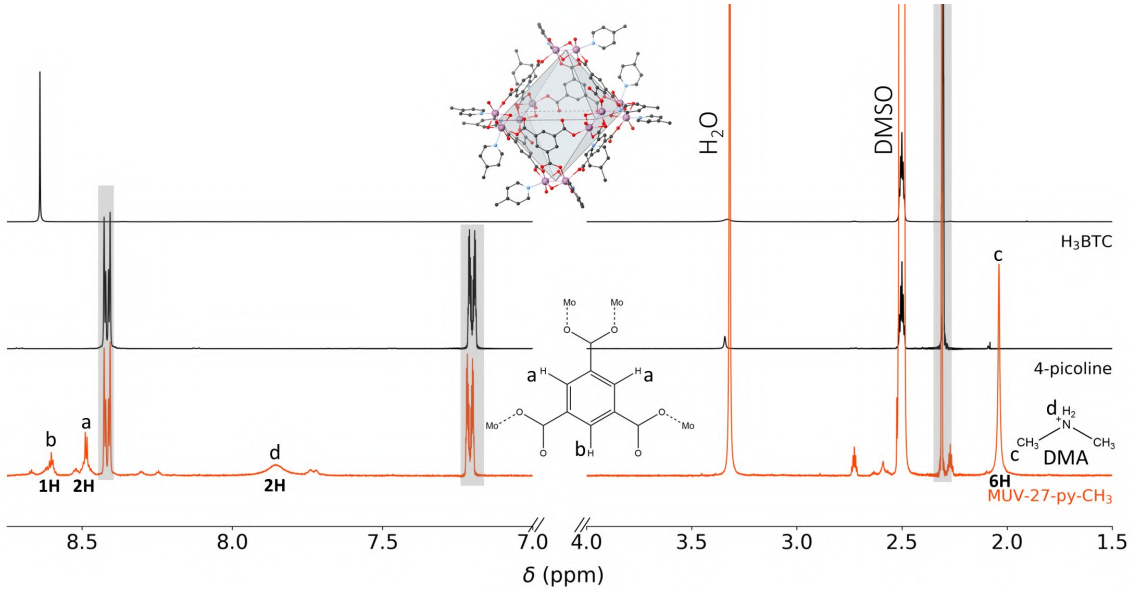

Figure S24. ^{1}H NMR of **MUV-27-py-CH$_3$** (DMSO-d_6, 300 MHz).

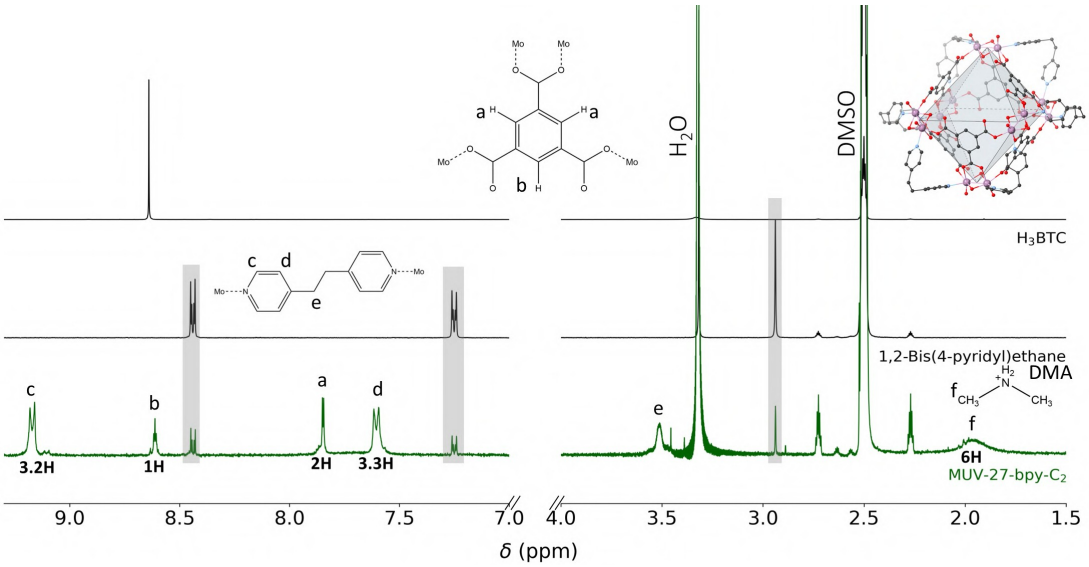

Figure S25. ^{1}H NMR of **MUV-27-bpy-C$_2$** (DMSO-d$_6$, 300 MHz).

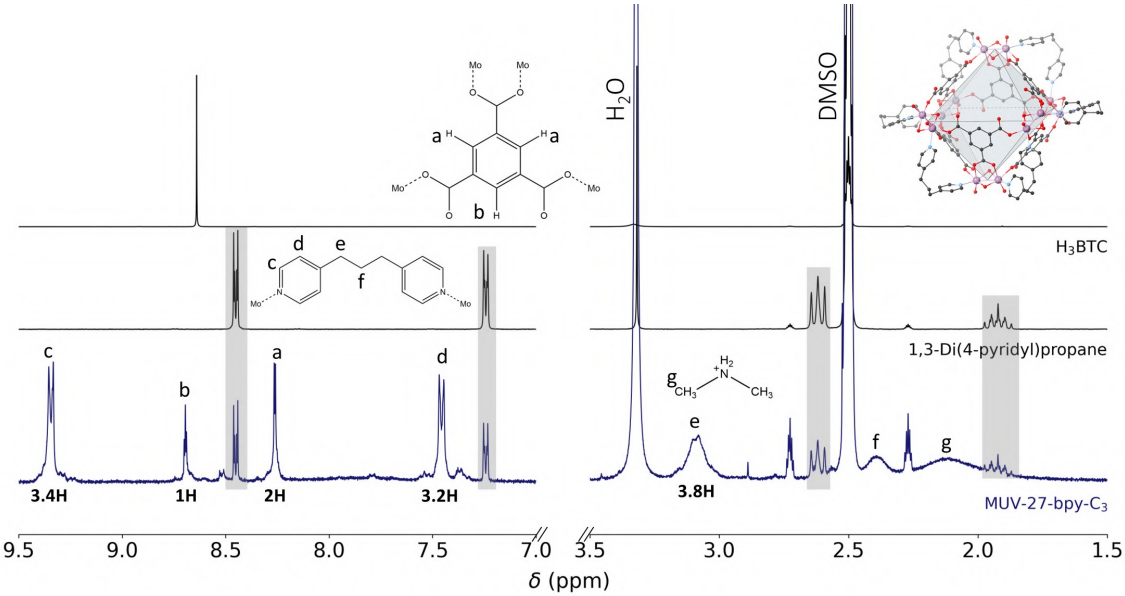

Figure S26. ^{1}H NMR of **MUV-27-bpy-C$_3$** (DMSO-d$_6$, 300 MHz).

S9.5 TGA of activated samples

Thermogravimetric Analysis (TGA) was performed on the activated **MUV-27** (Figure S27). All MOCs displayed an appreciable thermal stability that was suitable for removing DCM at 80°C, with a degradation starting at 120 °C for **MUV-27-py** and **MUV-27-py-CH_3**, and at 165 °C for the others. The measurements also showed the absence of DMF as no mass decrease was observed around 150 °C, which confirmed the activation of the samples.

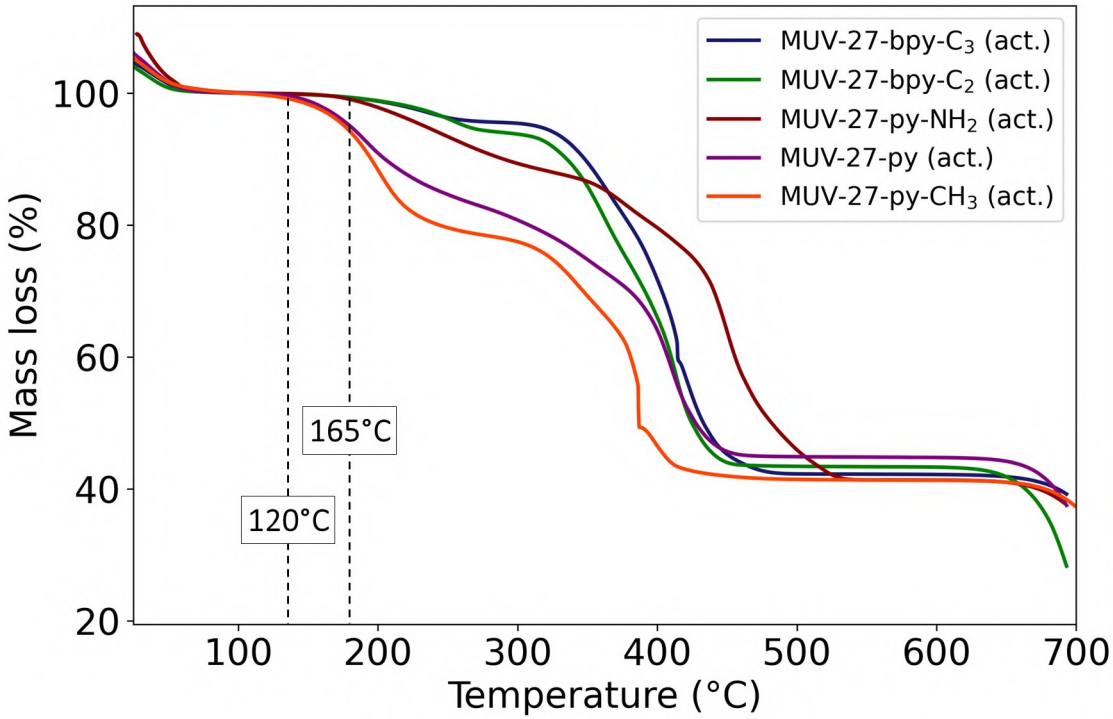

Figure S27. TGA of **MUV-27 (act.)**.

S10 Gas sorption

Activation of the samples was achieved by first washing the material with CH_2Cl_2 three times and immersion in CH_2Cl_2 during two days. Subsequently, the sample was air-dried before being fully activated at 80°C under vacuum for 3h. N_2 and CO_2 adsorption isotherms were carried out at 77 and 273 K respectively, on a Tristar II Plus Micromeritics sorptometer.

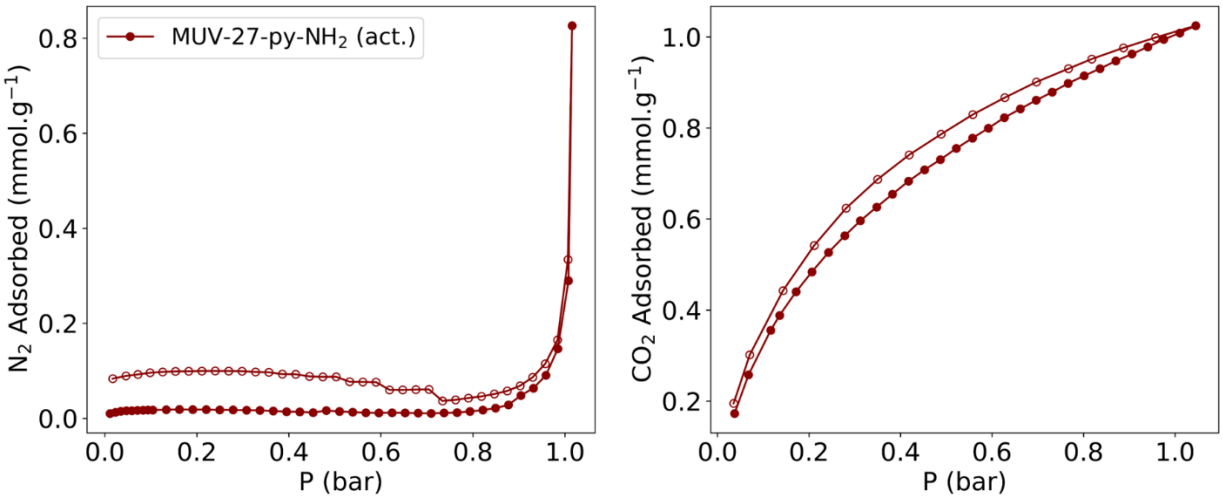

Figure S28. N_2 and CO_2 adsorption isotherms of activated **MUV-27-py-NH_2**, at 77 and 273 K respectively.

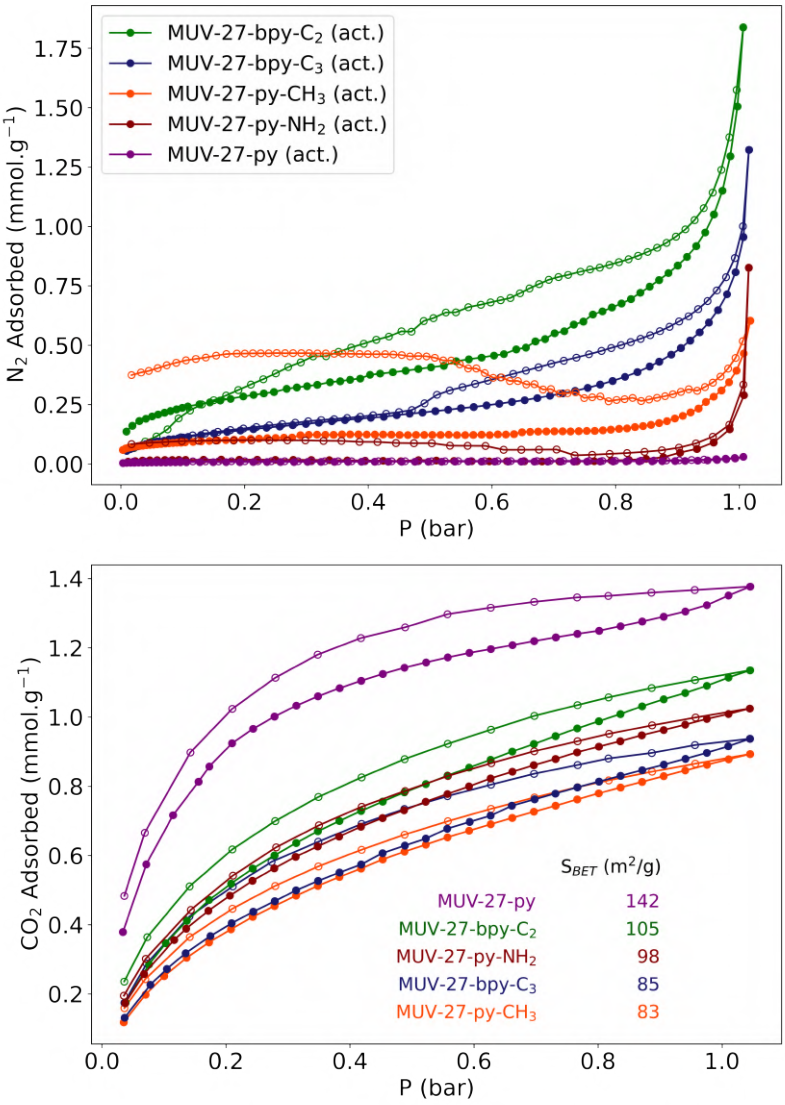

Figure S29. N_2 and CO_2 adsorption isotherms of activated **MUV-27** cages, at 77 and 273 K respectively.

S11 Post-synthetic modifications

We conducted post-synthetic modifications (PSMs) on **MUV-27-py** and **MUV-27-py-CH$_3$** in DMF, by exchanging the terminal pyridine ligands with those used in this work.

All the PSMs followed the same procedure. **MUV-27-py** (10 mg, $2.5 \cdot 10^{-3}$ mmol) or **MUV-27-py-CH$_3$** (10 mg, $2.4 \cdot 10^{-3}$ mmol) was mixed with either pyridine (0.1 ml, 1.24 mmol), 4-picoline (50 µL, 0.51 mmol), 4-aminopyridine (10 mg, 0.11 mmol), 1,2-bis(4-pyridyl)ethane (10 mg, 0.05 mmol) or 1,3-di(4-pyridyl)propane (10 mg, 0.05 mmol) in 4 mL DMF. The orange suspension was stirred at 50 °C overnight. The remaining solid was washed with DMF (3 x 2 mL) and dried under vacuum.

The quantitative substitution has been confirmed with IR (Figure S30) and ^{1}H NMR in DMSO (Figure S31) The crystallinity of the materials was also probed by PXRD, showing different results depending on the ligands used (Figure S32) All the characterization has been performed on the dried materials after being washed with DMF. The analysis is compared to the starting cage on top of each figure (**MUV-27-py** or **MUV-27-py-CH$_3$**), and to the corresponding **MUV-27** obtained through the direct synthetic pathway.

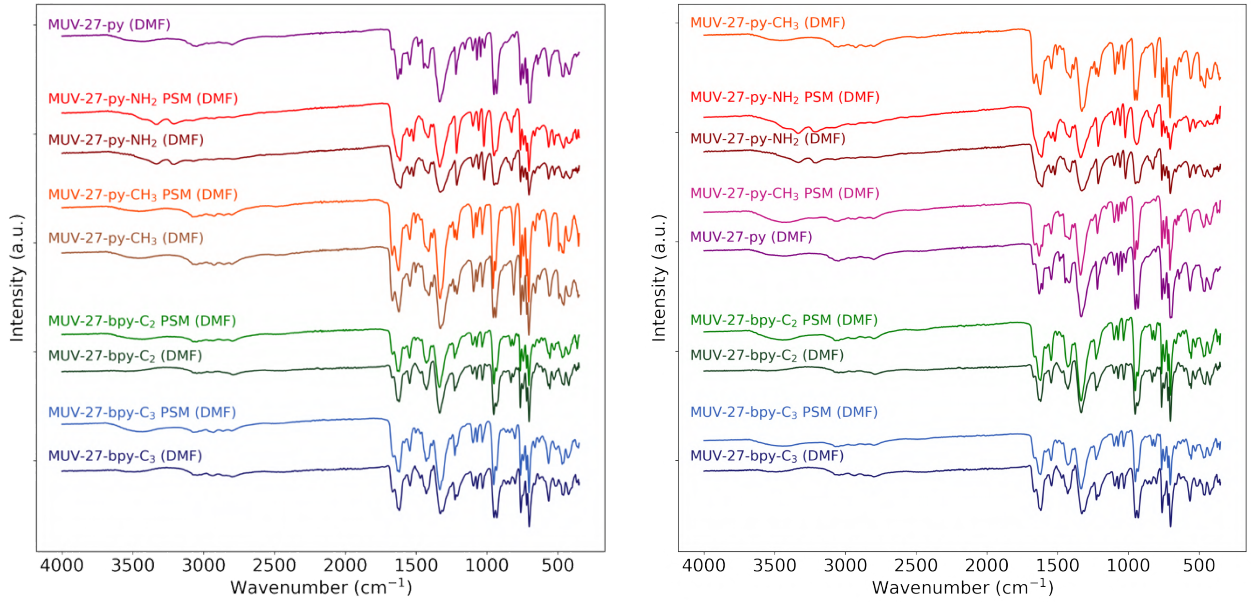

Figure S30. IR of the cages resulting from the PSM of **MUV-27** (a) and **MUV-27-py-CH$_3$** (b).

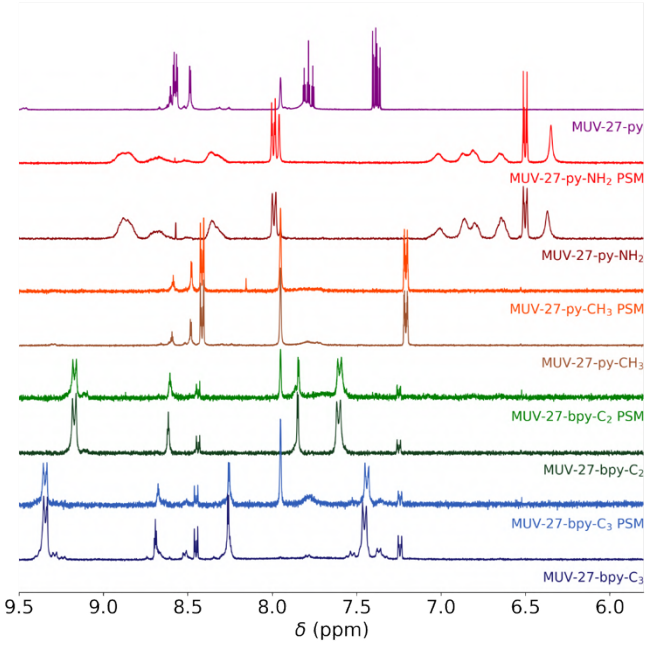

(a)

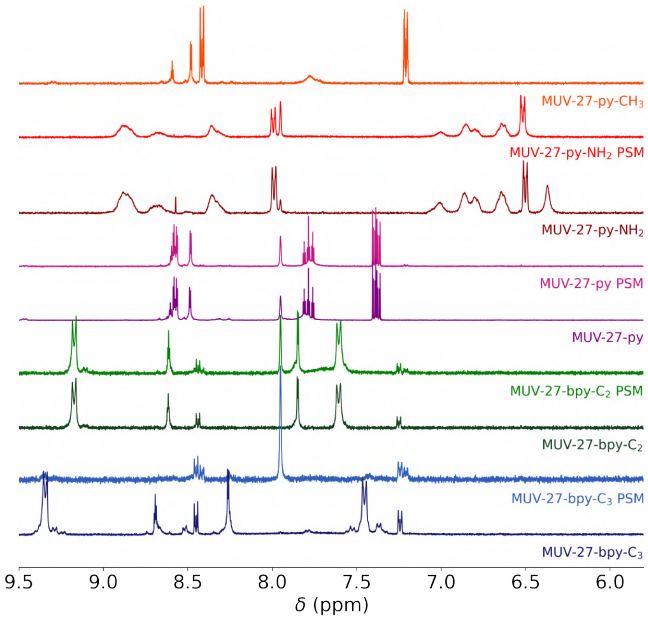

(b)

Figure S31. ^{1}H NMR (DMSO-d_6, 300 MHz) of the cages resulting from the PSM of **MUV-27-py** (a) and **MUV-27-py-CH$_3$** (b).

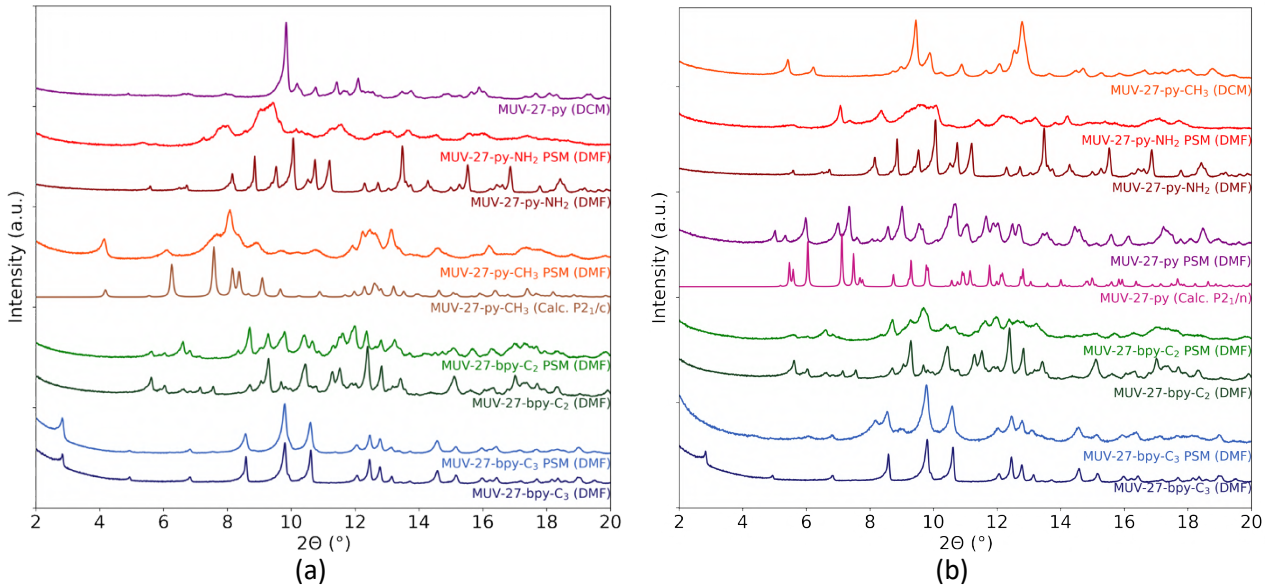

Figure S32. PXRD of the cages resulting from the PSM of **MUV-27-py** (a) and **MUV-27-py-CH$_3$** (b).

S12 References

[1] G. M. Sheldrick, *Acta Crystallogr. Sect. C*, 2015, **71**, 3–8.

[2] O. V. Dolomanov, L. J. Bourhis, R. J. Gildea, J. A. K. Howard, H. Puschmann, *J. Appl. Crystallogr.*, 2009, **42**, 339–341

[3] E. Pretsch, P. Bühlmann, M. Badertscher, *Structure determination of organic compounds: tables of spectral data*, Springer, Berlin, 4th edn., 2009.

[4] K. I. Hadjiivanov, D. A. Panayotov, M. Y. Mihaylov, E. Z. Ivanova, K. K. Chakarova, S. M. Andonova, N. L. Drenchev, *Chem. Rev.* 2021, **121**, 1286–1424.

[5] F. A. Cotton, D. L. Hunter, L. Ricard, R. Weiss, *J. Coord. Chem.*, 1974, **3**, 259–261.

[6] N. Panagiotou, K. Evangelou, A. Psalti, N. Varnava, G. K. Angeli, P. N. Trikalitis, J. C. Plakatouras, T. Lazarides, A. J. Tasiopoulos, *Mol. Syst. Des. Eng*, 2020, **5**, 1077–1087.